© 2020. Published by The Company of Biologists Ltd | Development (2020) 147, dev190553. doi:10.1242/dev.190553

RESEARCH ARTICLE

Perturbation analysis of a multi-morphogen Turing reaction-diffusion stripe patterning system reveals key regulatory interactions

Andrew D. Economou[1,*,‡], Nicholas A. M. Monk[2] and Jeremy B. A. Green[1,‡]

ABSTRACT

Periodic patterning is widespread in development and can be modelled by reaction-diffusion (RD) processes. However, minimal two-component RD descriptions are vastly simpler than the multi-molecular events that actually occur and are often hard to relate to real interactions measured experimentally. Addressing these issues, we investigated the periodic striped patterning of the rugae (transverse ridges) in the mammalian oral palate, focusing on multiple previously implicated pathways: FGF, Hh, Wnt and BMP. For each, we experimentally identified spatial patterns of activity and distinct responses of the system to inhibition. Through numerical and analytical approaches, we were able to constrain substantially the number of network structures consistent with the data. Determination of the dynamics of pattern appearance further revealed its initiation by 'activators' FGF and Wnt, and 'inhibitor' Hh, whereas BMP and mesenchyme-specific-FGF signalling were incorporated once stripes were formed. This further limited the number of possible networks. Experimental constraint thus limited the number of possible minimal networks to 154, just 0.004% of the number of possible diffusion-driven instability networks. Together, these studies articulate the principles of multi-morphogen RD patterning and demonstrate the utility of perturbation analysis for constraining RD systems.

This article has an associated 'The people behind the papers' interview.

KEY WORDS: Morphogens, Palate, Patterning, Reaction-diffusion, Rugae

INTRODUCTION

The generation of anatomy by self-organisation remains one of the most important subjects in the study of biology. It has acquired new importance as a guiding feature of regenerative medicine and the modelling of disease processes by the creation of self-organising organoids from stem cells (Werner et al., 2017). Setting aside mechanical self-organisation, a central idea of how self-organisation occurs chemically is that of reaction-diffusion (RD). In Turing's initial formulation, an initially stable system of two or more interacting morphogens can be destabilised (i.e. generate non-uniform distributions) into a periodic pattern through diffusion (Turing, 1952). This is referred to as a diffusion-driven instability (DDI). Gierer and Meinhardt later refined Turing's ideas and, among several refinements, introduced the formulation of the RD system as a system consisting of a slow-diffusing activator and fast-diffusing inhibitor (Meinhardt, 2012). Since the 1970s, numerous examples of RD behaviour have been described and analysed, and more recently the methods of molecular biology and biochemistry have identified a number of morphogen pairs, which are generally protein growth factors or growth-factor-binding proteins, that fit Turing's and Meinhardt's minimal description (e.g. Economou et al., 2012; Jung et al., 1998; Michon et al., 2008; Mou et al., 2006; Sick et al., 2006).

One aspect of self-organisation that has been set aside hitherto is that, as we now know, large proportions of the genome and proteome are devoted to regulation. Consequently, minimal systems must be expanded if they are to capture this complexity where it is functionally relevant. The extension of RD systems to include multiple morphogens and even non-diffusible components (Celliere et al., 2012; Klika et al., 2012; Marcon et al., 2016; Raspopovic et al., 2014) opens up a Pandora's box of possible descriptions of self-patterning systems. It raises the issue of what level of description is usefully interpretable and, importantly, experimentally tractable, such that empirical data and theory can be compared. We suggest that conceptually and pharmacologically, a usefully intelligible and accessible level of description is the signalling pathway: typically, this puts a family of protein growth factor ligands (e.g. the FGFs) together with their common receptors, transducers and target genes into a single unit. This provides a potentially happy balance between, on the one hand, the abstraction of a pure two-component morphogen system, the 'morphogens' of which bear little relationship to the single specific diffusible chemical species envisaged by Turing or even specific growth factors, and, on the other hand, the overwhelming complexity of an 'omic molecular network, the intelligibility of which would inevitably require dimensional reduction in any case.

Taking this level as our motivating principle [while acknowledging that it is a first approximation (see Discussion)], we contemplate how far one can get in defining a model (i.e. a network topology) of key interactions that can capture the behaviour of the system, when considering multiple signalling pathways. We analyse the periodic pattern that generates the transverse ridges on the roof of the mouse palate, the rugae, a striped pattern that we previously showed to exhibit RD system behaviour (Economou et al., 2012). Using chemical inhibitors and pathway target expression analysis together with analytical and numerical simulation strategies, we were able to identify topological motifs

[1]Department of Craniofacial Development & Stem Cell Biology, King's College London, London, SE1 9RT, UK. [2]School of Mathematics and Statistics, University of Sheffield, Sheffield, S3 7RH, UK.
*Present address: Developmental Signalling Laboratory, The Francis Crick Institute, 1 Midland Rd, Somers Town, London NW1 1AT, UK.

‡Authors for correspondence (jeremy.green@kcl.ac.uk; andrew.economou@crick.ac.uk)

A.D.E., 0000-0002-5193-0748; N.A.M.M., 0000-0002-5465-4857; J.B.A.G., 0000-0002-6102-2620

Handling Editor: Paul François
Received 12 March 2020; Accepted 11 September 2020

Development (2020) 147, dev190553. doi:10.1242/dev.190553

that are predictive of the behaviour of the system, regardless of the number of components considered in the network. Through further consideration of the dynamics of pattern formation, we have constrained the model possibilities to a small number of consistent topologies. In doing so, we identify a useful theory-experiment dialogue that generates specific hypotheses amenable to practical progress in understanding the dynamic behaviours of this example of a self-organising RD system.

RESULTS

Chemical inhibitors implicate FGF, hedgehog, Wnt and BMP pathways in periodic ruga patterning

We previously showed that the periodic stripes of expression of the sonic hedgehog (*Shh*) gene in the mouse mid-gestation palate depend on the Hh pathway itself as an 'inhibitor' and the FGF pathway as an 'activator' (Economou et al., 2012). We were deliberately agnostic about the specific FGF ligand-receptor pair that was crucial because multiple FGFs and FGF receptors are expressed in the palate (Porntaveetus et al., 2010). Both FGF and SHH are, by a number of experimental criteria, secreted diffusible morphogens (Bökel and Brand, 2013; Dessaud et al., 2007). As we acknowledged, there were already published data implicating Wnt and potentially BMP as additional morphogens (Lin et al., 2011; Welsh and O'Brien, 2009). To go beyond the simple two-component description of the patterning network, we sought first to determine the requirement for each of these four morphogen pathways using an established explant system, as before. We exposed embryonic (E) day 13.5 palatal explants for 24 h to cyclopamine (a hedgehog pathway inhibitor), SU-5402 (a FGF pathway inhibitor), IWP-2 (a Wnt pathway inhibitor) and dorsomorphin (a BMP pathway inhibitor), and tested the effect of these pathway-specific inhibitors on the pattern. Efficacy of these treatments was confirmed by probing for expression of direct transcriptional targets of each pathway: *Spry1*, *Ptch1*, *Lef1* and *Id1*, respectively (Economou et al., 2012; Fig. S1).

We used the stripes of *Shh* expression as our readout of the pattern (although in principle, any of the components could be used as a readout). Fig. 1A shows that inhibition of each of the four pathways has an effect on the *Shh* expression stripes. Through careful quantification (Figs S2, S3), we could demonstrate that although some inhibitors changed the number of *Shh* stripes, none of the inhibitors changed the position of the stripes (and therefore the wavelength of the pattern) relative to controls (Fig. S3A,B,E). Rather, inhibition changed the width and *Shh* staining intensity of stripes (Fig. S3C-E). Specifically, dorsomorphin intensified and broadened the stripes similar to what we previously reported for cyclopamine, whereas IWP-2 narrowed and weakened them. FGF inhibition by SU-5402 also weakened the stripes, as previously reported (Economou et al., 2012), but careful inspection over a number of trials also revealed consistent broadening as well as

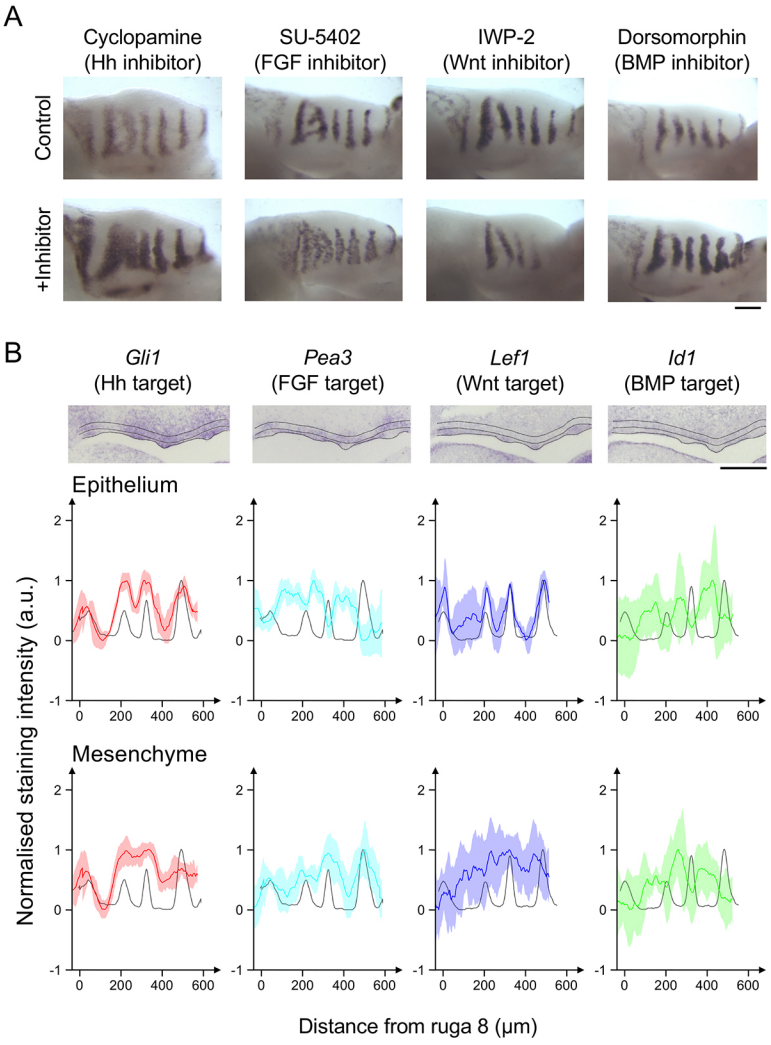

Fig. 1. Target expression and responses to inhibitors reveal involvement of Hh, FGF, Wnt and BMP pathways in periodic rugae patterning. (A) *Shh in situ* hybridisations on E13.5 palatal shelf explants cultured for 24 h in the specified small molecule inhibitor contralateral shelves as vehicle controls. Anterior to the right, medial up. (B) *In situ* hybridisation of sagittal sections of E13.5 palatal shelf for specified genes. Dotted lines illustrate the extent of the palatal epithelium and the underlying mesenchyme used for quantifications. Anterior to the right. The intensity profile averaged across the palatal shelf shown for each specimen from which the illustrated *in situ* is taken for the gene of interest (coloured trace) and *Shh* (grey trace) for the epithelium and mesenchyme. Shaded areas represent 1 s.d. around the gene of interest (for clarity of presentation the variation around *Shh* trace is not shown). For each marker, the number of specimens showing the observed pattern (essentially the number of specimens from which the kymographs in Fig. 6 were made) are: *Shh*, 114; *Gli1*, 42; *Pea3*, 41; *Lef1*, 41; and *Id1*, 34. a.u., arbitrary units. Scale bars: 200 μm.

Development (2020) 147, dev190553. doi:10.1242/dev.190553

weakening (Fig. 1A, Fig. S4). In some cases, posterior and anterior stripes differed in the magnitude of their response. On cyclopamine or SU-5402 treatment, posterior rugae appeared to widen more than anterior rugae, in some cases to the point of fusing with their neighbours (Fig. S3B,C), whereas on IWP-2 treatment, anterior rugae decrease in staining intensity more than posterior rugae, and in some cases to below the detection threshold leading to the apparent loss of stripes (Fig. S3B,D). However, although the magnitude of response could vary along the palate, the direction of response was the same across all *Shh* stripes (Fig. S3E). These results confirm that all four pathways contribute to the formation of the ruga pattern, and their inhibition changes the width and intensity of stripes but not the wavelength of the pattern.

We focused our attention on the anterior stripes (black points in Fig. S3C,D), which were already established before the addition of the inhibitor (as opposed to the posterior stripes, which were in a region of new stripe formation) and which we previously demonstrated were maintained by an RD mechanism through their ability to bifurcate on the removal of a neighbouring stripe (Economou et al., 2012). Although these stripes showed a weaker response to the inhibition of Hh and FGF signalling, and a stronger response to the inhibition of Wnt signalling than the posterior stripes, we speculate that all stripes involve the same RD mechanism and that these differences in magnitude relate to the difference between perturbing an already established steady-state pattern versus perturbing a non-steady-state region in which an unpatterned state is undergoing destabilisation.

Transcriptional pathway targets are expressed periodically and in different spatial phases

Although each of the pathway ligands are casually referred to in the literature as a morphogen, in the RD sense any of these could in fact be a uniform permissive component of the system rather than part of the periodicity-generating network. To be an RD-type patterning morphogen, the activity of its pathway must also be periodic. To determine where each of these pathways is active, we analysed well-established direct transcriptional targets of their respective transduction pathways (Fig. 1B, Fig. S5). Using pathway targets as the operational measure of pathway activity avoids the complications of multiple ligands, receptors and transduction components as discussed above. We found that each of the pathways had periodic outputs. Where available, additional target markers were tested and gave the same periodic pattern (Fig. S6). As expected, Hh target expression was in the same spatial phase as *Shh* in both epithelium and mesenchyme. Surprisingly, FGF signalling was in-phase with the *Shh* stripes in the mesenchyme but out-of-phase in the epithelium. This reconciles our previous description of FGF activity as being in-phase with the *Shh* stripes (Economou et al., 2012) with a previous report describing it as out-of-phase (Porntaveetus et al., 2010). It also means that FGF signalling must be functioning as effectively two different pathways (defining a pathway as its transcriptional end-point). We refer to these pathways as mesenchymal FGF (mFGF) and epithelial FGF (eFGF). Based on expression patterns, these are most likely to be FGF10/FGFR1 and FGF3/FGFR2 ligand/receptor pairs, respectively (Porntaveetus et al., 2010). Wnt target expression was in-phase in the epithelium and undetectable in the mesenchyme, whereas BMP signalling was out-of-phase in both layers (Fig. 1B). In summary, Hh, mFGF and Wnt (pathways) are in-phase with the rugae, and eFGF and BMP (pathways) are out-of-phase. The above findings show that each of the pathways is periodic and are therefore, by definition, part of a periodic pattern-generating network.

Multiple two-component RD networks are consistent with the phase and perturbation data

We then investigated how four or potentially five components can be wired together in a regulatory network that can generate the observed spatial pattern. One potentially simplifying approach is to consider whether the topology of this system (i.e. the network, technically a directed graph, in which chemical components are linked by activation or inhibition arrows) could effectively be described as a classical two-component RD system, which would consist of two 'master morphogens', with the other components serving as intermediates [so-called 'mediators' (Cho et al., 2011)] between them. This would be the case if the exact topology of a two-component system between two master morphogens was preserved in a larger system. Effectively, interactions between master morphogens in the two-component system would be expanded by passing through a series of mediators in which the net sign of the interactions is the same (Fig. S7A). Any pair of morphogens could potentially support a two-component system [if 'in-phase' by a classical activator-inhibitor (AI), or if 'out-of-phase' by a substrate-depletion (SD) configuration].

We therefore turned to perturbation analysis as a way of constraining possible network topologies. Using simple linear equations, we modelled the effects of perturbing either component in both classical two-component AI and SD systems. We investigated how a series of waves, generated by a two-component RD network from noisy initial conditions, would respond to the inhibition of each component. Preliminary investigations (Fig. S8) indicated that although the pattern of waves could be lost under strong inhibition, the series of waves could be preserved (including the wave number) if inhibition strength was reduced (Fig. S8D,E). However, upon inhibition, either the amplitude or the absolute level of the waves was shifted up or down. It should be noted that in some instances, the waves appeared bounded. For example, if a wave shifted up, only the troughs of the wave moved up, whereas the peaks did not move noticeably, and vice versa if the wave shifted down. (This appeared to be the case for the auto-activating component of a two-component RD system, where to form a stable series of waves the upper and lower production rates were bounded.) In these bounded cases in particular, the upward or downward shift in wave position was associated with a stripe widening or narrowing, respectively (Fig. S8F,G). The maintenance of wave number along with changes in width and intensity was reminiscent of the changes in *Shh* stripes seen in our inhibitor-treated explant cultures.

As the behaviour of the waves upon inhibition could be described as upward or downward shifts, we could capture it as shifts in the mean level of each component. Therefore, we generated 1000 random parameter sets consistent with the conditions for DDI for both AI and SD networks, and only considering parameter sets that could produce a stable series of waves, we determined the change in the mean component level upon inhibition (Fig. 2A, Fig. S9), ensuring that wave number was maintained after inhibition (Table S1). We confirmed that, for almost all parameter sets, the change in mean component level appeared to be the result of a shift in wave amplitude or absolute level, as illustrated in Fig. S8F,G (see also Table S1). We then compared the results with the effects on established spatial patterns of experimentally inhibiting Wnt, BMP or Hh itself, considering first all four possible two-component systems containing the Hh pathway (our readout) and excluding FGF [where two nodes are inhibited simultaneously requiring a different analysis (see below)]. We found that for both Wnt-Hh and BMP-Hh systems, one of the two possible two-component models was consistent with the data (Fig. 2B). However, there exists no three-

Development (2020) 147, dev190553. doi:10.1242/dev.190553

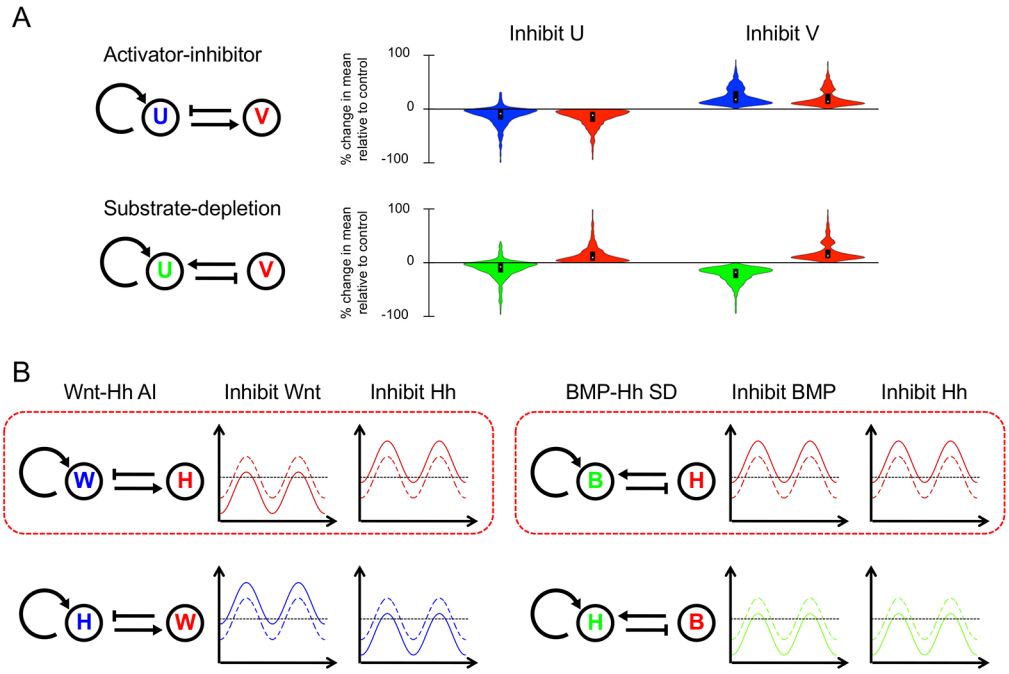

Fig. 2. Numerical simulation of RD patterning inhibition for two-component systems. (A) Violin plots showing percentage change in the mean level of components U and V in illustrated AI and SD RD networks upon inhibition of the response to morphogens U and V in RD simulations (plots for inhibition of production are shown in Fig. S9). (B) Networks showing the two possible configurations of Wnt-Hh AI systems and BMP-Hh SD systems, with components coloured according to the equivalent component in A. Associated with each network is a schematic of the response of Hh upon inhibition of each component in the network, based on the predominant response in the simulations. Solid lines indicate levels after inhibition, with dashed lines representing uninhibited states. Horizontal dotted lines represent an arbitrary detection threshold. The two topologies that have responses to inhibition that replicate the experimental observations (see Fig. 1A) are highlighted with a red box. B, BMP; H, Hh; W, Wnt.

component Wnt-BMP-Hh network which can be interpreted as both a master Wnt-Hh AI topology with BMP mediating a single interaction, and a master BMP-Hh SD topology with Wnt mediating a single interaction (Fig. 2, Fig. S7B,C). This showed that our system (probably like most real systems) cannot be accurately described as falling into either one of the two classical AI or SD classes.

Analysis and numerical modelling identifies well-connected network topologies capable of non-oscillating diffusion-driven instability

The above results showed that modelling this system requires consideration of higher order (i.e. greater than two-component) networks. Therefore, we next investigated whether any three-component networks could be found that were consistent with the spatial pattern and perturbation data. There are 3^9=19,683 possible three-component network topologies, as each component can interact with the two others and itself (nine types of interaction) and each interaction can be positive, negative or zero (Fig. S10). Considering that all components have some degradation rate, and therefore have some level of negative self-interaction, we only considered the distinction between topologies with positive self-interactions and those without them. This reduces the total number of possible topologies to $2^3\times3^6$=5832. [These different topologies incidentally place different constraints on diffusion, as discussed by Marcon et al. (2016).]

To go further, we resorted to numerical methods because, unlike for the two-component system, there is not a well-established relationship between network topology and spatial patterning for three-component networks (Scholes et al., 2019). Three-component RD systems were considered by White and Gilligan in the context of hosts, parasites and hyperparasites (White and Gilligan, 1998), in which they described criteria that determine which such systems generate DDI, as well as criteria to distinguish temporally stable from oscillating systems. More recently, related analyses, including graph-based approaches, have been applied to developmental periodic patterning (Marcon et al., 2016) and general RD systems (Diego et al., 2018; Scholes et al., 2019). We systematically screened parameter ranges around known values published for biological RD systems (Nakamasu et al., 2009) and applied the White and Gilligan (1998) criteria for DDI in a three-component model. Out of 242,121,642 parameter sets (9 interactions×7 values for each×6 different choices for which morphogens have high or low diffusion values) searched we found a subset of 653,574 parameter sets that gave DDI. The signs of the parameters define specific topologies. As the rugae form as stable stripes of gene expression and tissue thickening (Economou et al., 2013, 2012), our first observational constraint was that the stripes we see are non-oscillating. We recovered 1492 topologies giving non-oscillating DDI (see Materials and Methods for details). A second constraint was that inhibition of any of the components would perturb the pattern. This implied that every node (morphogen) in the network outputs as well as inputs, making the network 'strongly connected' (Marcon et al., 2016). We recovered 1396 strongly connected network topologies. Among these, the four possible phase relationships (all-in-phase or each one of the three out-of-phase with the other two) could each be generated by 498 different topologies (with some topologies capable of generating more than one possible phase relationship depending on parameter values).

To investigate the 498 topologies in a given phase group, we generated 'stalactite' plots according to Cotterell and Sharpe (2010). In this representation, each topology is shown as a point linked to all other topologies that differ from it by the gain/loss of one edge, with each row corresponding to the total number of edges. Topologies at

Development (2020) 147, dev190553. doi:10.1242/dev.190553

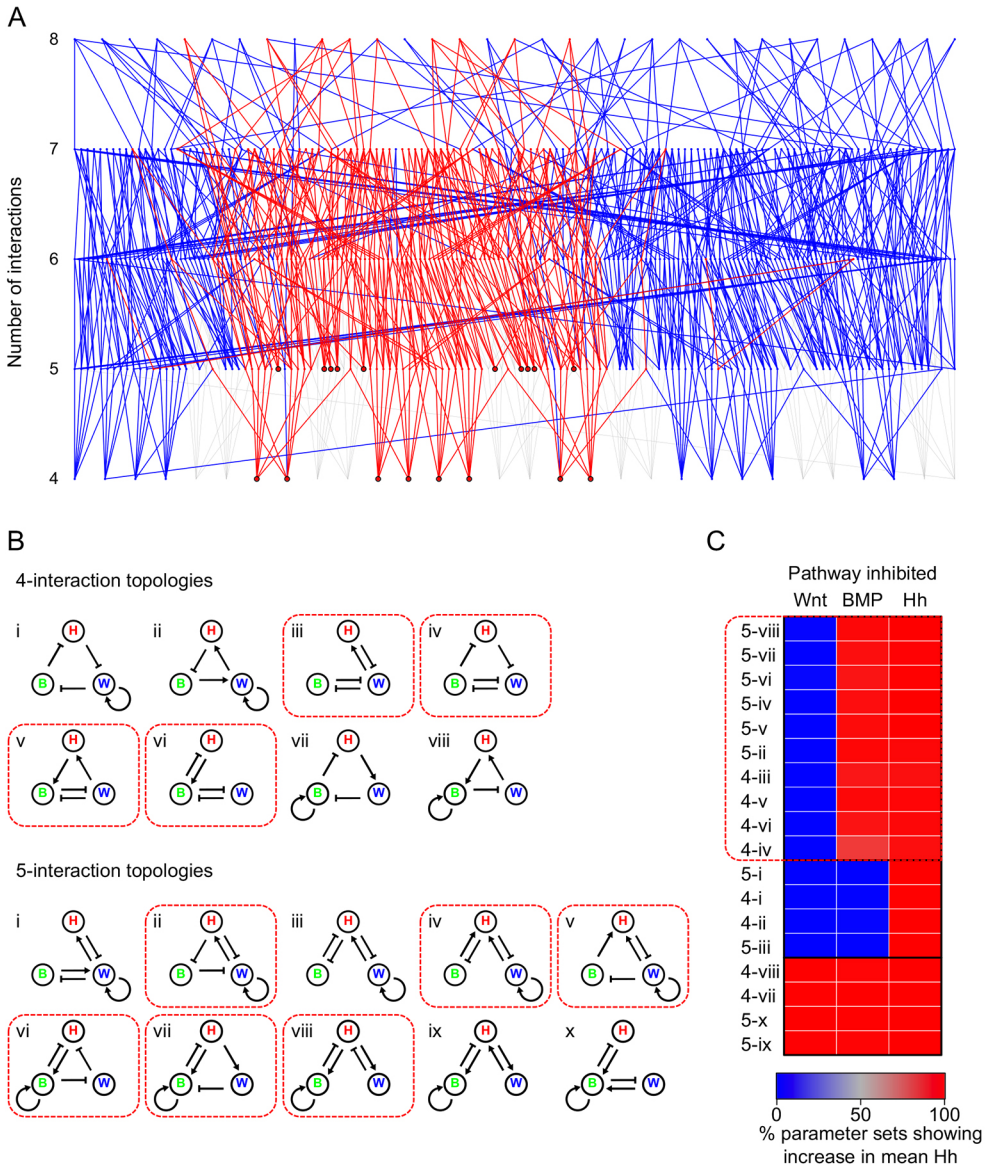

Fig. 3. 'Stalactite plot' and numerical simulation identifying subsets of three-component RD systems and their behaviours under inhibition. (A) Topology atlas for the phase group of the three-component network identified in the parameter search, which is consistent with the spatial pattern of Wnt, BMP and Hh. Topologies that can be recovered with fast-diffusing Hh and slow-diffusing Wnt and BMP are in blue. Out of the 45 strongly connected topologies that are found at the bottom of the stalactites, the 18 that are also consistent with the diffusion constraints are outlined in black. For completeness, not strongly-connected topologies are shown in grey along with their relationship to the strongly connected topologies. (B) Graphs showing the 18 Wnt-BMP-Hh networks divided into four-interaction and five-interaction networks. Within each group, networks are numbered according to their position from left to right in A. (C) Heat map showing the percentage of parameter sets in which the level of Hh increases in response to the inhibition of each component in the network in RD simulations. Topologies are grouped according to hierarchical clustering (see Fig. S10). The ten topologies that have a response that is consistent with the experimental data are highlighted with a red box, as are the network diagrams in B. B, BMP; H, Hh; W, Wnt.

the base of each stalactite, of which there were 45 for each phase group, represent those that are distinct (non-overlapping) and possess only non-redundant interactions (Fig. 3A). It should be noted that these topologies are slightly different to the minimal topologies defined by Diego et al. (2018) as we assume that all biological components have some degradation rate, and therefore do not include these interactions.

Spatial phase and perturbation outcomes further constrain the number of possible real networks

We could now begin to consider real morphogens as nodes in the identified topologies, to investigate which topologies could correspond, first, to the observed spatial phase relationships and, second, to likely diffusivities. We considered three-node networks consisting of Hh, Wnt and BMP. We knew the phase relationship of these from direct observation of the targets shown in Fig. 1: Hh and Wnt activities are in-phase with the rugae and BMP activity is out-of-phase. This constraint identified a specific phase group of 45 topologies as relevant to our system. As for diffusivities, to simplify the analysis we first set Hh as the fast-diffusing pathway compared with the other two, consistent with its role in our two-component analyses (Fig. 2B). (We show below that this provisional assumption is ultimately not required for the selection of networks consistent with the experiment.) These phase and diffusivity constraints reduced the number of working topologies down to just 18 (Fig. 3A,B).

With these 18 topologies, we now compared their predicted behaviour under perturbation with the experimental results using numerical simulations similar to those described above (see Materials and Methods for details). Inhibiting each component for 1000 randomly chosen DDI parameterisations of each topology revealed three groups of characteristic responses to inhibitions (Fig. 3C, Fig. S11, Table S2). Ten out of the 18 networks showed Hh pathway responses consistent with the experimentally observed changes in *Shh* expression (boxed in Fig. 3C).

Identification of feedback loop signs enables prediction of network behaviour under perturbation

From several thousand conceivable networks, the above analytical, numerical and experimental methods identified just ten three-component minimally connected topologies that captured the experimentally observed periodicity, phase and perturbation responses of three of the five components identified as active in

Development (2020) 147, dev190553. doi:10.1242/dev.190553

this system. We will refer to these as 'valid' networks. How might this help us discover what networks would be valid that include all five components, and potentially '*n*' additional components? It has been suggested that general rules for biological circuit behaviour can be inferred from analysis of the signs of the embedded feedback loops (Tyson and Novak, 2010). We therefore examined whether this approach might be applied to our RD networks. We observed that our valid three-component networks contained the same feedback loops as the two perturbation-consistent two-component networks (Fig. 2B). In the four-interaction networks, Wnt and BMP are in positive feedback loops by mutual inhibition, whereas Hh is always only in a negative feedback loop (Wnt and BMP can also be found in the negative feedback loop), and in the five-interaction networks, Wnt and BMP are still in a positive feedback loop through (direct or indirect) mutual inhibition, whereas the exact interactions, and therefore the feedback loops of either two-component system, are embedded in the network (Fig. 3B, Fig. S12 indicate the loops). In other words, the behaviour of the network, including under perturbation, is embedded in the product of the signs of the 'arrows', i.e. the signs of the reaction term coefficients. Indeed, Marcon et al. (2016) and Diego et al. (2018) recently demonstrated that the formation of patterns in RD systems is dependent on these destabilising positive feedback and stabilising negative feedback loops. To investigate whether the response to perturbation is also determined by these loops, we analysed the relationship between reaction terms (i.e. the RD equations without the diffusion terms) and the behaviour of components in response to perturbation. We showed that this has a consistent mathematical form (asymptotic curves), which enables the sign of the perturbation response (as opposed to its precise magnitude) to be predicted as a relatively simple set of conditions fulfilling or not fulfilling certain inequalities (see Appendix S1, section 2.1). Through comparison with simulations of the full RD system (see Appendix S1, section 2.2) we found that for all but very small perturbations (in which diffusion can dominate) or very large perturbations (in which RD breaks down altogether), that it is indeed possible to predict the behaviour of an RD-competent network from its reaction terms alone. Analytical considerations reinforce this conclusion (see Appendix S1, section 2.2).

To further explore the relationship between the network topology and the response to perturbation, we expressed the terms in the inequalities as functions of the combination of signs of the reaction terms (i.e. feedback loops) in *n*-component systems, thus predicting the effects on perturbation of any given RD system component, depending on its participation in positive and/or negative feedback loops (see Appendix S1, section 3). We were able to use this

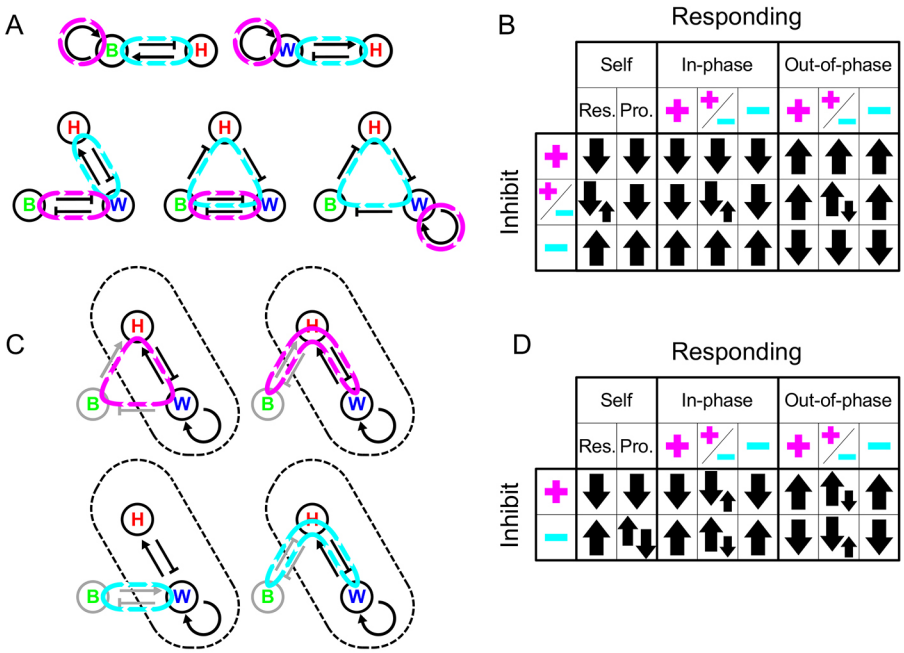

Fig. 4. Identification of feedback loops and resulting behaviours under inhibition for three-component RD systems. (A) Illustrative two- and three-component networks showing minimal feedback requirements for RD of one or more components forming a single positive feedback loop (highlighted in magenta), with a negative feedback loop being formed through at least one additional component (highlighted in cyan). (B) Summary constraint table showing the response of components in such a minimal network to the inhibition of a component found in either the positive feedback loop alone (magenta 'plus' sign), negative feedback loop alone (cyan 'minus' sign) or both ('plus' and 'minus'), depending on which loop they are in and the phase relative to the inhibited component ('in-phase' or 'out-of-phase'). For the response of a component to its own inhibition ('self'), the inhibition of response ('res.') and production ('pro.') are shown. Upward pointing arrows indicate an increase in the level of a component, whereas downward arrows indicate a decrease. Two arrows of equal size show when the system is unconstrained. Where opposing large and small arrows are shown, the system behaves according to the large arrows, apart from under certain topologies (see Appendix S1, section 4) in which the reverse is seen for certain components. Although components are not constrained, different components showing the unconstrained response are coupled to one another. (C) Illustrative examples showing how additional components can be integrated into a minimal RD system outside of the 'core' RD network by forming external loops. External components and interactions are shown in grey, either forming positive or negative feedback loops with the core positive feedback loop (highlighted in magenta and cyan, respectively). Core RD network outlined with dashes. (D) Summary constraint table showing the response of components in such a network to the inhibition of a component that provides either additional positive feedback (magenta 'plus' sign) or additional negative feedback (cyan 'minus' sign) to the core positive feedback loop. The table shows how this depends on which loop in the core network they are in [response (Res.); production (Pro.); +, ± or –] and the phase relative to the inhibited component. Symbols as in B. For a subset of topologies in which a component is in both loops see Appendix S1, section 4. B, BMP; H, Hh; W, Wnt.

Development (2020) 147, dev190553. doi:10.1242/dev.190553

approach to analyse how the response of components to inhibition in the system changes upon stepwise addition of new nodes (components) (see Appendix S1, section 4). In brief, and consistent with the results of an analysis into the topological requirements for RD by Diego et al. (2018), an RD system requires that for an n-node system, there needs to be a positive feedback loop through a maximum of $n-m$ nodes and a negative feedback loop through the remaining m nodes (provided $n>m\geq 1$), and at least one node must be in both loops. Examples of loops in two-node (classical RD) and three-node systems are shown in Fig. 4A. With these conditions in mind, one can predict outcomes of perturbations of each type of node included in these loops (Fig. 4B). However, the above conditions allow for networks in which these loops go through only a subset of nodes. The predictions of outcomes of perturbations in Fig. 4B therefore need not apply. Further analysis (described in Appendix S1, section 4) generated predictions of what happens to components represented by nodes outside these RD-defining 'core' loops (Fig. 4C,D). We found the effects of inhibition of these 'non-core' components to be mostly similar, but not identical, to those of inhibition of core components. [This means that sometimes alternative 'cores' in a given network will produce different perturbation responses (see Discussion below).]

Incidentally, this feedback loop decomposition can also help explain the seemingly counterintuitive nature of pattern formation in some topologies. For example, topology iv in Fig. 3B can produce a periodic pattern despite only consisting of negative interactions. In this topology, positive feedback loop of the RD is produced by the mutual inhibition between Wnt and BMP, whereas the negative feedback loop comes from the cycle of three inhibitory interactions between Wnt, BMP and Hh.

We applied these rules for perturbation responses and effects of node addition to the 45 Wnt-BMP-Hh networks discussed above that fulfilled the requirements of diffusion-driven instability and the observed phase relationships. Systematically identifying all possible loop combinations (Fig. S13) enabled the prediction of the responses of each component to any inhibition using the constraint tables in Fig. 4. This showed that the observed perturbation responses corresponded to the same ten topologies as in Fig. 3 but in this case without the prior assumption that Hh was the fast-diffusing component.

The effect of inhibition of FGF can now be reconsidered. As the effect on *Shh* expression was neither net increase nor net decrease, we considered topologies in which eFGF and mFGF acted in opposition. Simulation with a parameterisation of the very simple network of this kind depicted in Fig. 5A showed that a blended increase and decrease leading to a flatter waveform was indeed obtained (Fig. 5B). Thus, an RD system with two FGFs, each having opposite effects on *Shh*, can account for our experimental observations.

We considered all possible five-component topologies with loops required for DDI with the sign of links constrained by their phase relationship (see Appendix S1, section 4). Specifically, we first identified all possible sets of core topologies (i.e. all subnetworks of two to five components that have the minimal number of interactions sufficient for RD). For each core, all possible combinations for wiring-in the remaining components were recovered (see Materials and Methods for details). This yielded 39,755 unique minimal topologies. Prediction of their responses to inhibition revealed that, of these, 3945 were consistent with our experimental perturbation results. Fig. 5C,D depicts these topologies in terms of the interactions (arrows) between the five components. Although some interactions are different in different topologies, some are the same or absent for all topologies [e.g. the input of mFGF to eFGF indicated in the column second from the right are inhibitory (cyan) or absent (white) in all topologies].

Developmental dynamics of stripe appearance reveal an eFGF-Wnt-Hh 'core' network with mFGF/BMP incorporation after stripe establishment

What further experimental data could constrain potential network topologies? We turned to temporal behaviour of the rugal system. We conducted a large number of *in situ* hybridisations on adjacent sections from a long time-series of specimens, spatially registering multiple specimens to the stripes of *Shh* expression. Because the pattern arises through monotonic linear growth (Economou et al., 2012), we could temporally order and space our specimens (see Fig. S14 and Materials and Methods for details on converting palatal lengths to time). This allowed us to determine the kinetics of the onset of stripe formation for each of the pathway markers relative to *Shh* expression onset (Fig. 6A-E). Moreover, as tissue growth occurs immediately anterior to ruga 8, it follows that older tissue lies more anterior in the palate. Therefore, by using anteroposterior (AP) position as a proxy for time and correlating the different transcriptional target genes with *Shh* at increasing anterior positions, we could follow the sequence of signalling events in ruga formation by determining where (and therefore when) the different transcriptional targets come into (or out-of) phase with *Shh* (Fig. S15).

The loss of FGF target *Pea3* (also known as *Etv4*) in the epithelium and expression of the Wnt target *Lef1* are the first instances of markers establishing their spatial patterns, and are simultaneous with the onset of *Shh* transcription (Fig. 6C-E). On the other hand, the increase of Hh target *Gli1*, downregulation of BMP target *Id1* and the increase of FGF target *Pea3* in the mesenchyme lag the onset of *Shh* expression. However, the correlation analysis also shows that the onset of *Shh* expression (and therefore the downregulation of *Pea3* and the upregulation of *Lef1*) is concomitant with a transient negative correlation and, therefore, reduced expression of *Gli1*. This transient period of reduced Hh signalling at the onset of stripe formation in a region of tissue growth is consistent with a role for Hh in providing negative feedback.

What do the dynamic data mean for our networks? As eFGF and Wnt responses are the first movers and move simultaneously, they must form a core positive feedback loop together with Hh providing the negative feedback loop necessary for RD. As BMP and mFGF responses trail Hh, they cannot be part of the core positive feedback loop that destabilises the system. Applying these constraints to the 3945 topologies that were consistent with the experimentally observed phase relations and responses to perturbation gave 154 topologies consistent with the observed dynamics (Fig. 7A,B). This number constitutes 0.004% of the total 39,755 DDI minimal topologies. All of these are subsets of the same set of regulatory interactions (Fig. 7C), comprising one of four possible Wnt-eFGF-Hh cores, with BMP and mFGF providing additional interactions.

DISCUSSION

We have shown that five classical morphogen pathways periodically pattern the rugae and have identified a relatively small number of potential RD network topologies, and an even smaller number of consistent regulatory interactions between nodes within such networks. The modelling, combined with the experimentation thus far, suggests, although of course does not prove, potentially direct molecular interactions between specific pathway-induced transcription factors and target enhancer sites in the genes encoding the other morphogens.

Development (2020) 147, dev190553. doi:10.1242/dev.190553

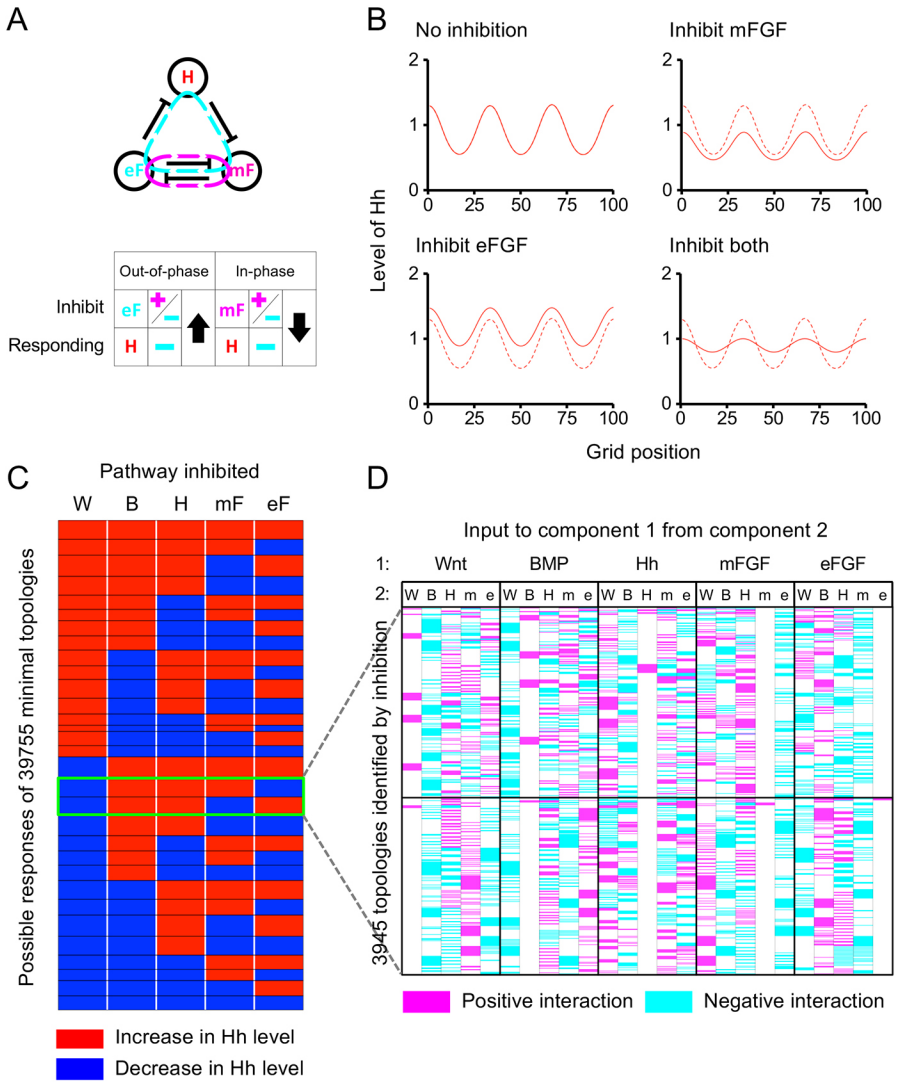

Fig. 5. Integration of two out-of-phase FGF morphogens explains FGF-inhibition effects and allows the prediction of behaviours under inhibition of five-component RD systems. (A) Example of a network where the inhibition of epithelial FGF (eF) and mesenchymal FGF (mF) would be predicted to have opposing effects on the levels of Hh (H) according to analysis of reaction terms, alongside an illustration of how this is determined through the constraints imposed by the different feedback loops in the system [positive feedback loop alone (magenta 'plus' sign), negative feedback loop alone (cyan 'minus' sign) or both ('plus' and 'minus'), depending on which loop they are in and the phase relative to the inhibited component ('in-phase' or 'out-of-phase')]. Positive and negative feedback loops are shown in magenta and cyan, respectively. (B) Simulation of single and combined inhibition of the two FGF components (dashed lines indicate uninhibited state). Simulations carried out as detailed in Materials and Methods. u_1 is mF, u_2 is eF and u_3 is H, with a_{12}=−0.019, a_{13}=−0.034, a_{21}=−0.019, a_{32}=−0.022, b_1=0.064, b_2=0.037, b_3=0.068, c_1=0.004, c_2=0.011, c_3=0.039, $fmax_1$=0.008, $fmax_2$=0.022, $fmax_3$=0.072, D_1=1.03, D_2=1.71 and D_3=7.63. Where not specified a_{ij}=0. Initial conditions drawn from a random distribution, as described in Materials and Methods. (C) Map showing all possible responses of Hh to inhibition of each of the five components for all 39,755 predicted minimal topologies (red, increase in Hh; blue, decrease in Hh). Topologies arranged into 31 different groups of responses, outlined in black. Two sets of responses that constitute 3945 topologies showing the observed responses (Wnt down, BMP up, Hh up, and mFGF and eFGF opposing responses) highlighted in the green box. (D) Map showing the interactions making up the 3945 topologies identified by perturbation analysis (positive interactions in magenta, negative in cyan, no interaction in white). Horizontal black line separates topologies giving different patterns of responses of Hh in response to mFGF and eFGF inhibition (upper group of topologies correspond to the upper group of highlighted topologies in C). B, BMP; H, Hh; W, Wnt.

This study highlights more generally the ways in which experimental data can be used to challenge RD models in a mammalian tissue context. In particular, we have shown that the effects of relatively small acute perturbations to spatial patterns that have already formed are highly constraining on plausible network topologies. This suggests that similar inhibitor studies can be a useful complement to 'knockout' genetics in understanding these dynamical systems. We also gained constraining information from the dynamic (temporal) evolution of the system during embryonic development. This was facilitated by the sequential appearance of the stripes, which is a peculiarity of this rugal palate system. In many periodic patterns, such as, for example, the appearance of cartilage ring-patterning stripes in the developing trachea (Sala et al., 2011), stripes appear simultaneously and so identifying leading and lagging genes would require more quantitative measurements.

It is striking that increasing component number (even at an arbitrarily chosen level) reduces constraint very rapidly. Notably, at the three-component level there is a small part of parameter space for which networks give behaviours that do not conform to the minimal topologies from which they are derived. How this grows and whether

Development (2020) 147, dev190553. doi:10.1242/dev.190553

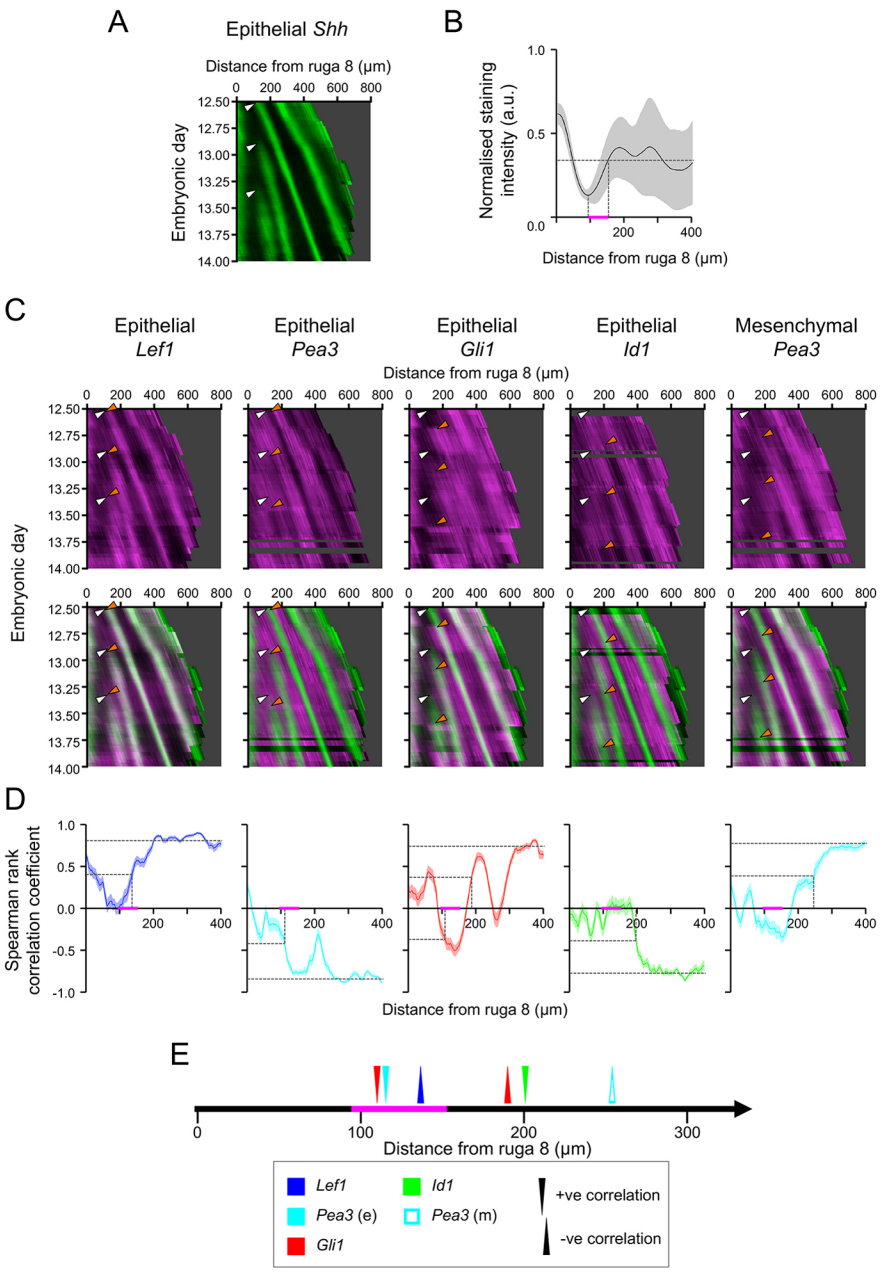

Fig. 6. Periodic gene expression kymographs reveal an early Wnt-eFGF-Hh initiating 'core' system with mFGF and BMP integrated later. (A) Kymograph showing the pattern of expression of *Shh* through time. White arrowheads indicate the approximate onset of *Shh* expression for each ruga. (B) Plot of mean normalised intensity of *Shh* staining for each AP position relative to ruga 8. The magenta bar denotes the period of onset of *Shh* expression, bounded by the minimum in staining intensity and the position at which the staining intensity plateaus (vertical dashed lines). Horizontal dashed line shows level at which *Shh* intensity plateaus (as determined by the mean intensity of the anterior third of the palate). Shaded area represents 1 s.d. (C) Kymographs showing the pattern of expression of indicated target genes through time (magenta) and their expression relative to *Shh* (green) for rugae 3, 4 and 5. White arrowheads as in A, and orange arrowheads indicate approximate positions of the change in the expression pattern of each target gene associated with each ruga. Mesenchymal *Gli1* and *Id1* expression resemble the epithelial patterns (see Fig. S16) (horizontal dark bands in the red channel are stages for which too few specimens were obtained to allow interpolation). (D) Plot of the Spearman's rank correlation coefficient for the intensity of *Shh* staining and the marked target gene across all time points for each position relative to ruga 8, indicating when, relative to the onset of *Shh* expression, the spatial pattern for each target gene emerges. Horizontal dashed lines represent maximal correlation coefficient, calculated over the anterior third of the palate (Fig. S15D) and half this value. Vertical dashed lines represent AP position where this level is first reached. Lower dashed lines for *Gli1* show where the half maximal level is reached for the opposite correlation (i.e. out-of-phase rather than in-phase). Shaded area represents 95% confidence interval from bootstrapping (see Materials and Methods). The magenta bar represents the period of onset of *Shh* expression, as determined in B. (E) Sequence whereby different targets come into (upward pointing arrowheads) or out-of (downward pointing arrowheads) phase with *Shh* relative to the distance from ruga 8, based on the correlation analysis in D. The magenta bar represents the period of onset of *Shh* expression, as determined in B. a.u., arbitrary units.

it could be important at higher orders is not clear. However, the 'black boxing' of whole pathways into single nodes provides a way of rationally reducing the system complexity in a way that makes biological sense. It remains an open question as to how to integrate this way of thinking with omic datasets. There is a significant body of work on analysis and simplification of complex regulatory networks and some thought has been given to RD processes within these (Mincheva and Roussel, 2012). However, practical application of these methods with experimental input is still in its infancy. Meanwhile, caution must be applied. For example, in the limb, modelling and experiments have shown that BMP2 and its transduction, manifested as phosphorylated Smad proteins, are spatially out-of-phase (Raspopovic et al., 2014). This highlights the fact that defining the activity of a pathway as expression of its direct transcriptional targets is a choice rather than a necessity.

Apart from the computational aspects of our work, this study raises biological questions. Why, for example, does the patterning of the palate use five pathways when, in principle, two would do? More specifically in our system, why is the rugal pattern initiated with three morphogens but then incorporate an additional two? One possibility is that this provides a particular type of robustness to perturbations: yes, there are many targets whose mutation can affect the pattern, but there is also significant redundancy such that the modifications to the pattern are mostly relatively subtle. Another possibility is that each pathway provides an additional tuning of the pattern or setting up of signalling for downstream events such as differentiation. A completely opposite explanation is that all of the regulatory interactions exist in cells and are used elsewhere for multiple other purposes (for RD or not, and in pairs or not), and that the apparent 'overkill' in terms of numbers of pathways involved is merely because there is no evolutionary pressure to eliminate or suppress their role in the palate. More detailed analysis of the robustness properties of these networks and of the conservation of the regulatory interactions is needed to address these questions.

Development (2020) 147, dev190553. doi:10.1242/dev.190553

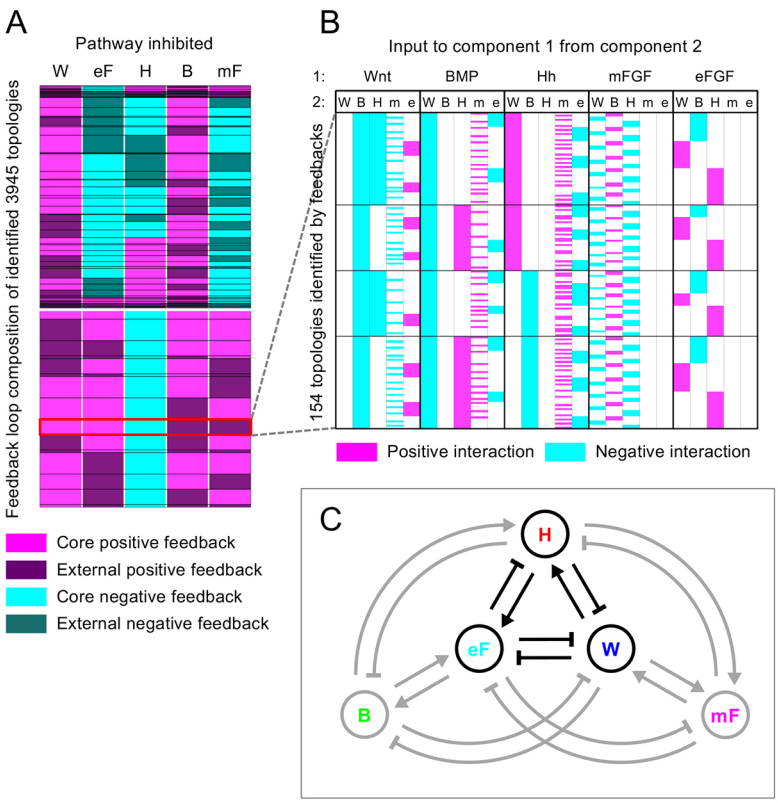

Fig. 7. Possible feedback loops and network topologies constrained by the experiment. (A) Map showing feedback loop structure of 3945 topologies by perturbation analysis (see Fig. 5C,D). Components involved in positive feedback are in magenta and those involved in negative feedback are in cyan, with components external to the core in dark. Horizontal white line separates topologies giving different patterns of responses of Hh in response to mFGF and eFGF inhibition (upper group of topologies correspond to upper group of highlighted topologies in Fig. 5C,D). Groups of topologies showing different patterns of feedback loops are outlined in black. A set of 154 topologies showing constraints on topology as determined by kinetic analysis (Wnt and eFGF as only core positive feedback components and Hh as core negative feedback component) boxed in red. (B) Map showing the interactions making up the 154 topologies identified by feedback loop analysis (positive interactions in magenta, negative in cyan, and no interaction in white). Horizontal black lines separate four groups of topologies with different interactions between the three core components Wnt, eFGF and Hh. (C) The 154 topologies identified in A and shown in B, all show the same signs of interactions where present. Summary network diagram showing the signs of the interactions found among these topologies. B, BMP; H, Hh; W, Wnt.

MATERIALS AND METHODS

Generation of embryos and explants

Wild-type CD1 mice (*Mus musculus*) were obtained and used according to protocols approved by the Institutional Animal Ethics Committee under UK Home Office Project and Personal Animal Licences. Embryos were harvested, staged, fixed and stained for whole-mount *in situ* hybridization using established methods. Palate explants from E13.5 embryos were made using 0.1 mm tungsten needles and cultured at 37°C in 5% CO_2 atmosphere for 24 h using the Trowell technique (Alfaqeeh and Tucker, 2013) in serum-free advanced Dulbecco's modified eagle media/F12 (GibcoBRL), 20 U/ml penicillin-streptomycin (GibcoBRL), 50 mM transferrin (Sigma-Aldrich) and 150 µg/ml ascorbic acid (Sigma-Aldrich). Chemical inhibitors were added at the beginning of the 24 h culture period at the following final concentrations: SU-5402 (Calbiochem) at 40 µM; cyclopamine (Sigma-Aldrich) at 20 µM; IWP-2 (Cambridge Bioscience/Cell Guidance Systems) at 50 µM; and dorsomorphin (Cayman Chemical) at 50 µM. Control palates were contralateral explants from the same embryo incubated with vehicle only. Experiments were repeated at least four times for each condition.

In situ hybridization

For sectioned *in situ* hybridization, fixed specimens were embedded in wax and serially sectioned (7 µm), with successive sections mounted on four different slides to allow different probes to be used on nearby/adjacent sections. Whole-mount and sectioned *in situ* hybridisations were conducted according to standard methods (Economou et al., 2012). Probes were gifts from colleagues obtained initially from authors of published references as follows: *Shh* (Echelard et al., 1993); *Lef1* (Gat et al., 1998); *Id1* (Rice et al., 2000); *Spry2* (Tefft et al., 1999); *Ptch1* (Goodrich et al., 1999); *Gli1* (Hui et al., 1994); *Etv4* (*Pea3*); *Etv5* (*Erm1*) (Chotteau-Lelièvre et al., 1997); and *Axin2* (Lustig et al., 2002). Whole-stained explants, placed in a minimum volume of PBS in wells cut into 1% agarose, were digitally imaged using a stereo dissecting microscope.

Identifying rugae in explant culture

To determine the number of rugal stripes of *Shh* expression, as well as their position, width and staining intensity, a 150 µm wide strip was drawn along the AP length of the palate through the region of the rugae. The mean greyscale level along the mediolateral axis at each AP position was determined, with rugae appearing as peaks in *Shh* intensity (note that as stronger intensity staining has a lower greyscale value, peaks in the array fall at greyscale minima). The AP boundaries of each ruga were taken at half the height from a rugal peak to the adjacent troughs. In some instances, rugae were closely spaced, leading to the fusion of rugal *Shh* peaks (as identified by the intensity of a trough being greater than one third the height of the peak to the next trough). For such fused blocks of rugae, boundaries were determined by interpolating between the outer well-identified boundaries and thresholding relative to this line. The bounds of ruga 1 were not calculated as the edge of the palate made necessary intensity measurements at the anterior unreliable. The position of each ruga was determined as the midpoint between the AP boundaries (apart from ruga 1 and 8, which were manually identified on each image), and ruga width as the difference between these boundaries. Ruga intensity was measured as the minimum greyscale value within the bounds of a ruga.

Quantifying the effect of inhibition

Rugae in inhibitor-treated explants were aligned to their contralateral controls by minimising the sum of the squared differences between the positions of ruga 1 and ruga 8. AP position was measured relative to the control ruga 8, and each ruga was paired with the closest ruga in the contralateral shelf. In some cases, a ruga could not be paired; for example, if the closest ruga in the control lay closer to another ruga in the treated. In such cases, if the position of the ruga aligned to an interrugal region in the contralateral, it was determined that the ruga had been lost upon inhibitor treatment (or the equivalent ruga was not inserted in the contralateral). In these cases the width was recorded as 0 µm and the intensity measured at the equivalent position in the interrugal region. Alternatively, if multiple rugae in the control aligned with the same ruga in an inhibitor-treated specimen, it was determined that multiple rugae had fused. In these cases, the width of the fused-region ruga was divided in proportion with the control rugae, and the intensity was taken within the bounds of these regions. To identify any differences associated with the addition of new rugae, posterior rugae were identified as ruga 8 and the next anterior ruga.

Development (2020) 147, dev190553. doi:10.1242/dev.190553

To determine how distributions of these different measurements shifted upon inhibitor treatment, the variation in the absence of inhibitor was determined. Position, width and intensity were measured for contralateral pairs of untreated explant, and the absolute displacement from having equal values between the two was calculated. The proportion of rugae that fell above or below one median displacement from equality was calculated for each measurement under each treatment.

Construction of target gene expression profiles

The mouse embryonic head was sectioned at 7 µm intervals in the sagittal aspect. For a given marker, *in situ* hybridization was performed on every fourth or fifth section, for the entire mediolateral extent of the rugae. Sections were imaged using a Zeiss Axioskop upright microscope with a 20× objective under both brightfield and phase contrast. To record the variation of relative expression along the AP axis of the palatal epithelium and underlying mesenchyme, the apical and basal extents of the epithelium were first manually traced on the phase contrast images (upon which unstained epithelium could be clearly seen) using ImageJ. We wrote a macro in ImageJ (see under profiles and kymographs at www.gitlab.com/adeconomou/ruga-patterning-quantifications-and-simulations) to return the relative staining intensity (as recorded in the bright-field images converted to 8-bit greyscale) within the traces along the epithelium (averaged across its thickness) and in the underlying 25 µm of mesenchyme. The basal-to-apical thickness of the epithelium was also captured. The position of ruga 3 within the trace was recorded manually. For a given palatal shelf, intensity profiles were made for all sections stained for a particular marker (sections damaged during the sectioning and staining process were excluded). Because the rugae were approximately parallel, it was sufficient to align the intensity profiles to the position of ruga 3 to obtain an average intensity profile along the AP axis of a palatal shelf (Fig. S5). Average intensity profiles were normalised, with the maximal signal intensity (darkest pixel value) taken as 1, and the minimal signal intensity (lightest pixel value) taken as 0.

Construction of kymographs

As the palatal epithelium extends along its AP axis through localised growth immediately anterior to ruga 8, the AP palatal distance between ruga 3 and ruga 8 was used to measure embryonic age (i.e. time). Embryo weights were recorded (in 25 mg bins) and first a high-resolution calibration curve was constructed relating embryonic weights to time-of-harvest for 412 embryos across 38 litters, as described by Peterka et al. (2002). Weights and rugae 3-to-8 distances of *in situ*-hybridised embryos could then be related to embryonic age through a second calibration curve (Fig. S14). Processing to make the kymographs was carried out using R Core Team (2013) (see code at www.gitlab.com/adeconomou/ruga-patterning-quantifications-and-simulations.git) as follows. To produce a smooth kymograph, normalised intensity profiles were positioned by time and aligned in the AP direction at ruga 3. A moving average (using a 0.2 day window) was calculated to smooth the intensity plot in the time axis. Where there were fewer than two traces in the window, no value was plotted. Finally, the kymograph was replotted as distance relative to ruga 8 (see sample dataset at www.gitlab.com/adeconomou/ruga-patterning-quantifications-and-simulations). For correlation analysis, Spearman's rank correlation coefficient was calculated between the normalised intensity of *Shh* and each target across 600 evenly spaced time points from E12.5 to E14.0, for all AP positions. The onset of periodic expression was taken as the position at which the correlation coefficient reached half of its final level (measured across the anterior one third of the palate). For all AP positions, 95% confidence intervals were calculated from 1000 bootstrap replicates.

Numerical simulations

RD systems were simulated in R using a piecewise linear model. (A detailed description of relevant code is given in Appendix S1 and the code itself is freely available from GitLab at www.gitlab.com/adeconomou/ruga-patterning-quantifications-and-simulations.git.)

The model was of the form:

$$\frac{\partial u_i}{\partial t} = f_i(u_1, u_2, \ldots, u_N) - c_i u_i + D_i \frac{\partial^2 u_i}{\partial x^2}, \quad i = 1, \ldots, N$$

$$f_i(u_1, u_2, \ldots, u_N) = \Phi\left(\sum_{j=1}^{N} a_{ij} u_j + b_i, fmax_i\right)$$

with

$$\Phi(z, fmax) = 0 \text{ for } z < 0$$

$$\Phi(z, fmax) = z \text{ for } 0 \le z \le fmax$$

$$\Phi(z, fmax) = fmax \text{ for } z > fmax.$$

The N variables $u_i(x, t)$, i=1,…,N, represent the concentrations of each component of the RD system as functions of time and a single spatial variable x (distance along the AP axis of the palate). The non-negative parameters c_i and D_i represent the degradation rate and diffusion coefficients of the components, respectively.

The function $f_i(u_1,\ldots,u_N)$, i=1,…,N, specifies the production rate of component i, which takes a non-negative value between 0 and $fmax_i$. We take this to be a piecewise linear function Φ of the weighted sum of all regulatory inputs, where the parameter a_{ij} represents the weight of the direct regulatory input from component j to component i (i.e. the sensitivity of the production rate of i to changes in the concentration of component j).

The qualitative form (topology) of an RD system is specified by the nature of the interactions between its components (positive, negative or no interaction). For any given topology, interaction parameters (a_{ij} where $i \neq j$) were either set to 0 (i.e. no interaction) or assigned a value at random from a uniform distribution between −1 and 1, with the sign determined by the nature (positive or negative) of the interaction. For self-interactions (a_{ij} where $i=j$), the composite parameter $a_{ii}-c_i$ was drawn from this uniform distribution, taking a negative weighting when there is no autoregulation (a_{ii}=0). When a component auto-activates, the parameter takes a positive value, with the weight of $-c_i$ also being drawn from the distribution. Diffusion coefficients (D_i) were drawn as the reciprocal of values from a uniform distribution between 1 and 10,000, meaning that at the lower end of the distribution, small differences would have a large effect on the diffusion range.

To assess whether a particular parameterization of the RD system would support the formation of spatial patterns through DDI, and what phase-type of pattern the parameterization could produce, the parameters were compared with the criteria for a DDI generating stable spatially periodic non-oscillating patterns described initially by White and Gilligan (1998) with some additional elaboration described in Appendix S1, section 1.

To ensure that spatially periodic solutions of the model do not take negative values, they must form around a positive spatially-uniform steady state (all u_i>0); to ensure this, appropriate production constants b_i are required (Raspopovic et al., 2014). Therefore, for parameter sets that support DDI, constant regulatory input terms (b_i) were calculated so that for each component, the spatially-uniform steady state concentration was fixed at 1. In order for the amplitude of patterns generated from linear RD to remain bounded, the production functions $f_i(u_1,\ldots,u_N)$ must be bounded (Shoji et al., 2003). We set the lower bound to be zero (production cannot be negative) and the upper bounds to be $fmax_i$. To ensure that the maximum production rates $fmax_i$ were greater than the production rate at steady state (so that the production rates at steady state are linear functions of their inputs), the $fmax_i$ were set randomly between 1.5× and 3× the magnitude of c_i.

RD simulations were run using a finite difference scheme with zero flux boundary conditions on a discrete one-dimensional grid of 100 positions. Parameter sets were scaled to ensure non-discretised spatially periodic solutions would be formed on the spatial domain used by comparing the wavelength and growth rate (as detailed in Appendix S1, section 1) with values known to fit within the simulation space and time to generate a scaling factor, and then using that factor to run an initial simulation from which spatial patterns could be measured and the parameters scaled more precisely.

Perturbation analysis

Scaled parameter sets were simulated as described above, with all grid positions initially drawn at random from a uniform distribution between −0.01 and 0.01 around the equilibrium point of the reaction term matrix of the RD system. For parameterisations in which a stable spatial pattern of 2 to 4.5 complete waves (to avoid discretisation) was established in the RD system, components were inhibited in one of two different ways. Inhibition of the receptor of a given morphogen (as seen for the inhibitors cyclopamine, SU-5402 and dorsomorphin, for example) was implemented as an equal proportional reduction of all interaction coefficients representing the response to that morphogen [so if the response to component u_j was inhibited, the values of a_{ij} were reduced by a factor $(1–\alpha)$ for all values of i]. Inhibition of the production of a component (e.g. IWP-2) was achieved by proportionately reducing the production term of that component by a factor $(1–\alpha)$ (see Appendix S1, section 2 for details). For all parameter sets, by successively reducing the strength of the inhibition parameter α by a factor of 0.25 from complete inhibition (α=1), we determined empirically for each pathway the maximum perturbation α_{max} that still allowed patterning but did not perturb the number of whole wavelengths or fail to achieve a stable amplitude. The test statistic for perturbation effects was the mean level for each component relative to an unperturbed run. To confirm that this readout accurately reflected an upward or downward shift in the wave, as was seen in the experimental system, the shift in the troughs and peaks of the waves, respectively, were also recorded: if an increase in mean was associated with an increase in the position of the wave troughs, or a decrease in the position of the wave peaks, it was determined that the wave had shifted upwards or downwards, respectively (Fig. S8F,G).

Topology search

For the three-component RD system, parameter space was systematically sampled to identify parameter sets and topologies capable of giving DDI. Each of the nine reaction parameters a_{ij} were varied linearly through seven values spread evenly around 0 to give a total of 40,353,607 parameter sets. Diffusion parameters were initially set as two fast and one slow or vice versa, although this requirement [based on the longstanding but recently overturned idea (Marcon et al., 2016) that this difference is essential] turned out not to be essential (see Results). DDI criteria for stable periodic non-oscillating patterns, as mentioned above and described in detail in Appendix S1, section 2, were applied.

Acknowledgements

We thank Atsushi Ohazama, Martyn Cobourne, Abigail Tucker, Albert Basson and David Rice for providing us with *in situ* probe constructs, and Attila Czikas-Nagy and Ton Coolen for critical reading of the manuscript.

Competing interests

The authors declare no competing or financial interests.

Author contributions

Conceptualization: A.D.E., J.B.A.G.; Methodology: A.D.E., N.A.M.M.; Software: A.D.E.; Validation: A.D.E.; Formal analysis: A.D.E.; Investigation: A.D.E.; Writing - original draft: A.D.E., J.B.A.G.; Writing - review & editing: A.D.E., N.A.M.M.; Visualization: A.D.E., J.B.A.G.; Supervision: J.B.A.G.; Project administration: J.B.A.G.; Funding acquisition: J.B.A.G.

Funding

This work was funded by the Biotechnology and Biological Sciences Research Council (BB/J009105/1 to J.B.A.G.). Deposited in PMC for immediate release.

Supplementary information

Supplementary information available online at
https://dev.biologists.org/lookup/doi/10.1242/dev.190553.supplemental

Peer Review History

The peer review history is available online at
https://dev.biologists.org/lookup/doi/10.1242/dev.190553.reviewer-comments.pdf

References

Alfaqeeh, S. A. and Tucker, A. S. (2013). The slice culture method for following development of tooth germs in explant culture. *J. Vis. Exp.* **10**, e50824. doi:10.3791/50824

Bökel, C. and Brand, M. (2013). Generation and interpretation of FGF morphogen gradients in vertebrates. *Curr. Opin. Genet. Dev.* **23**, 415-422. doi:10.1016/j.gde.2013.03.002

Celliere, G., Menshykau, D. and Iber, D. (2012). Simulations demonstrate a simple network to be sufficient to control branch point selection, smooth muscle and vasculature formation during lung branching morphogenesis. *Biol. Open* **1**, 775-788. doi:10.1242/bio.20121339

Cho, S.-W., Kwak, S., Woolley, T. E., Lee, M.-J., Kim, E.-J., Baker, R. E., Kim, H.-J., Shin, J.-S., Tickle, C., Maini, P. K. et al. (2011). Interactions between Shh, Sostdc1 and Wnt signaling and a new feedback loop for spatial patterning of the teeth. *Development* **138**, 1807-1816. doi:10.1242/dev.056051

Chotteau-Lelièvre, A., Desbiens, X., Pelczar, H., Defossez, P.-A. and de Launoit, Y. (1997). Differential expression patterns of the PEA3 group transcription factors through murine embryonic development. *Oncogene* **15**, 937-952. doi:10.1038/sj.onc.1201261

Cotterell, J. and Sharpe, J. (2010). An atlas of gene regulatory networks reveals multiple three-gene mechanisms for interpreting morphogen gradients. *Mol. Syst. Biol.* **6**, 425. doi:10.1038/msb.2010.74

Dessaud, E., Yang, L. L., Hill, K., Cox, B., Ulloa, F., Ribeiro, A., Mynett, A., Novitch, B. G. and Briscoe, J. (2007). Interpretation of the sonic hedgehog morphogen gradient by a temporal adaptation mechanism. *Nature* **450**, 717-720. doi:10.1038/nature06347

Diego, X., Marcon, L., Müller, P. and Sharpe, J. (2018). Key Features of turing systems are determined purely by network topology. *Phys. Rev. X* **8**, 021071. doi:10.1103/PhysRevX.8.021071

Echelard, Y., Epstein, D. J., St-Jacques, B., Shen, L., Mohler, J., McMahon, J. A. and McMahon, A. P. (1993). Sonic hedgehog, a member of a family of putative signaling molecules, is implicated in the regulation of CNS polarity. *Cell* **75**, 1417-1430. doi:10.1016/0092-8674(93)90627-3

Economou, A. D., Ohazama, A., Porntaveetus, T., Sharpe, P. T., Kondo, S., Basson, M. A., Gritli-Linde, A., Cobourne, M. T. and Green, J. B. A. (2012). Periodic stripe formation by a turing mechanism operating at growth zones in the mammalian palate. *Nat. Genet.* **44**, 348-351. doi:10.1038/ng.1090

Economou, A. D., Brock, L. J., Cobourne, M. T. and Green, J. B. A. (2013). Whole population cell analysis of a landmark-rich mammalian epithelium reveals multiple elongation mechanisms. *Development* **140**, 4740-4750. doi:10.1242/dev.096545

Gat, U., DasGupta, R., Degenstein, L. and Fuchs, E. (1998). De Novo hair follicle morphogenesis and hair tumors in mice expressing a truncated beta-catenin in skin. *Cell* **95**, 605-614. doi:10.1016/S0092-8674(00)81631-1

Goodrich, L. V., Jung, D., Higgins, K. M. and Scott, M. P. (1999). Overexpression of ptc1 inhibits induction of Shh target genes and prevents normal patterning in the neural tube. *Dev. Biol.* **211**, 323-334. doi:10.1006/dbio.1999.9311

Hui, C.-C., Slusarski, D., Platt, K. A., Holmgren, R. and Joyner, A. L. (1994). Expression of three mouse homologs of the Drosophila segment polarity gene cubitus interruptus, Gli, Gli-2, and Gli-3, in ectoderm- and mesoderm-derived tissues suggests multiple roles during postimplantation development. *Dev. Biol.* **162**, 402-413. doi:10.1006/dbio.1994.1097

Jung, H.-S., Francis-West, P. H., Widelitz, R. B., Jiang, T.-X., Ting-Berreth, S., Tickle, C., Wolpert, L. and Chuong, C.-M. (1998). Local inhibitory action of BMPs and their relationships with activators in feather formation: implications for periodic patterning. *Dev. Biol.* **196**, 11-23. doi:10.1006/dbio.1998.8850

Klika, V., Baker, R. E., Headon, D. and Gaffney, E. A. (2012). The influence of receptor-mediated interactions on reaction-diffusion mechanisms of cellular self-organisation. *Bull. Math. Biol.* **74**, 935-957. doi:10.1007/s11538-011-9699-4

Lin, C., Fisher, A. V., Yin, Y., Maruyama, T., Veith, G. M., Dhandha, M., Huang, G. J., Hsu, W. and Ma, L. (2011). The inductive role of Wnt-beta-Catenin signaling in the formation of oral apparatus. *Dev. Biol.* **356**, 40-50. doi:10.1016/j.ydbio.2011.05.002

Lustig, B., Jerchow, B., Sachs, M., Weiler, S., Pietsch, T., Karsten, U., van de Wetering, M., Clevers, H., Schlag, P. M., Birchmeier, W. et al. (2002). Negative feedback loop of Wnt signaling through upregulation of conductin/axin2 in colorectal and liver tumors. *Mol. Cell. Biol.* **22**, 1184-1193. doi:10.1128/MCB.22.4.1184-1193.2002

Marcon, L., Diego, X., Sharpe, J. and Müller, P. (2016). High-throughput mathematical analysis identifies turing networks for patterning with equally diffusing signals. *eLife* **5**, e14022. doi:10.7554/elife.14022

Meinhardt, H. (2012). Turing's theory of morphogenesis of 1952 and the subsequent discovery of the crucial role of local self-enhancement and long-range inhibition. *Interface Focus* **2**, 407-416. doi:10.1098/rsfs.2011.0097

Michon, F., Forest, L., Collomb, E., Demongeot, J. and Dhouailly, D. (2008). BMP2 and BMP7 play antagonistic roles in feather induction. *Development* **135**, 2797-2805. doi:10.1242/dev.018341

Mincheva, M. and Roussel, M. R. (2012). Turing-Hopf instability in biochemical reaction networks arising from pairs of subnetworks. *Math. Biosci.* **240**, 1-11. doi:10.1016/j.mbs.2012.05.007

Mou, C., Jackson, B., Schneider, P., Overbeek, P. A. and Headon, D. J. (2006). Generation of the primary hair follicle pattern. *Proc. Natl. Acad. Sci. USA* **103**, 9075-9080. doi:10.1073/pnas.0600825103

Nakamasu, A., Takahashi, G., Kanbe, A. and Kondo, S. (2009). Interactions between zebrafish pigment cells responsible for the generation of Turing patterns. *Proc. Natl. Acad. Sci. USA* **106**, 8429-8434. doi:10.1073/pnas.0808622106

Peterka, M., Lesot, H. and Peterková, R. (2002). Body weight in mouse embryos specifies staging of tooth development. *Connect. Tissue Res.* **43**, 186-190. doi:10.1080/03008200290000673

Porntaveetus, T., Oommen, S., Sharpe, P. T. and Ohazama, A. (2010). Expression of Fgf signalling pathway related genes during palatal rugae development in the mouse. *Gene Expr. Patterns* **10**, 193-198. doi:10.1016/j.gep.2010.03.004

R Core Team (2013). *R: A Language and Environment for Statistical Computing*. Vienna, Austria: R Foundation for Statistical Computing.

Raspopovic, J., Marcon, L., Russo, L. and Sharpe, J. (2014). Modeling digits. Digit patterning is controlled by a Bmp-Sox9-Wnt Turing network modulated by morphogen gradients. *Science* **345**, 566-570. doi:10.1126/science.1252960

Rice, D. P., Aberg, T., Chan, Y., Tang, Z., Kettunen, P. J., Pakarinen, L., Maxson, R. E. and Thesleff, I. (2000). Integration of FGF and TWIST in calvarial bone and suture development. *Development* **127**, 1845-1855.

Sala, F. G., Del Moral, P.-M., Tiozzo, C., Alam, D. A., Warburton, D., Grikscheit, T., Veltmaat, J. M. and Bellusci, S. (2011). FGF10 controls the patterning of the tracheal cartilage rings via Shh. *Development* **138**, 273-282. doi:10.1242/dev.051680

Scholes, N. S., Schnoerr, D., Isalan, M. and Stumpf, M. P. H. (2019). A comprehensive network atlas reveals that turing patterns are common but not robust. *Cell Syst.* **9**, 243-257.e4. doi:10.1016/j.cels.2019.07.007

Shoji, H., Iwasa, Y. and Kondo, S. (2003). Stripes, spots, or reversed spots in two-dimensional turing systems. *J. Theor. Biol.* **224**, 339-350. doi:10.1016/S0022-5193(03)00170-X

Sick, S., Reinker, S., Timmer, J. and Schlake, T. (2006). WNT and DKK determine hair follicle spacing through a reaction-diffusion mechanism. *Science* **314**, 1447-1450. doi:10.1126/science.1130088

Tefft, J. D., Lee, M., Smith, S., Leinwand, M., Zhao, J., Bringas, P., Jr., Crowe, D. L. and Warburton, D. (1999). Conserved function of mSpry-2, a murine homolog of Drosophila sprouty, which negatively modulates respiratory organogenesis. *Curr. Biol.* **9**, 219-222. doi:10.1016/S0960-9822(99)80094-3

Turing, A. M. (1952). The chemical basis of morphogenesis. *Philos. Trans. R. Soc. Lond. B Biol. Sci.* **237**, 37-72. doi:10.1098/rstb.1952.0012

Tyson, J. J. and Novák, B. (2010). Functional motifs in biochemical reaction networks. *Annu. Rev. Phys. Chem.* **61**, 219-240. doi:10.1146/annurev.physchem.012809.103457

Welsh, I. C. and O'Brien, T. P. (2009). Signaling integration in the rugae growth zone directs sequential SHH signaling center formation during the rostral outgrowth of the palate. *Dev. Biol.* **336**, 53-67. doi:10.1016/j.ydbio.2009.09.028

Werner, S., Vu, H. T.-K. and Rink, J. C. (2017). Self-organization in development, regeneration and organoids. *Curr. Opin. Cell Biol.* **44**, 102-109. doi:10.1016/j.ceb.2016.09.002

White, K. A. J. and Gilligan, C. A. (1998). Spatial heterogeneity in three species, plant–parasite–hyperparasite, systems. *Philos. Trans. R. Soc. Lond. B Biol. Sci.* **353**, 543-557. doi:10.1098/rstb.1998.0226

Supplementary Figures and Tables for Economou et al. " Perturbation analysis of a multi-morphogen Turing Reaction-Diffusion stripe patterning system reveals key regulatory interactions"

This document contains

- Supplementary Figures S1-S16 (pages 1-10)
- Supplementary Tables 1 and 2 (page 11)
- Supplementary Notes 1-4 (pages 12-45)

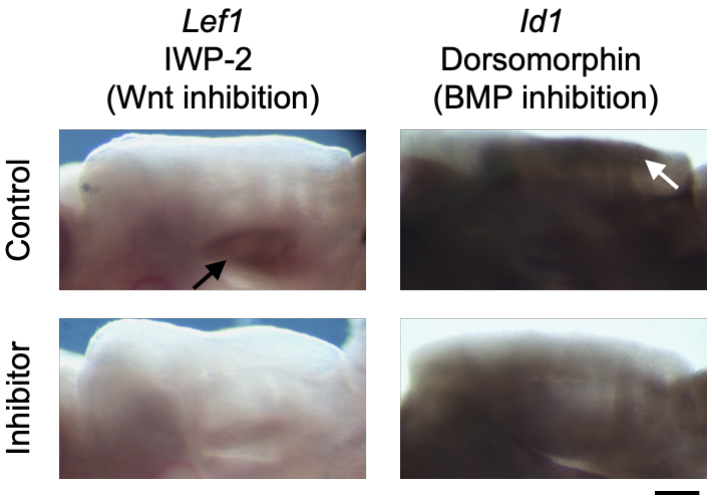

Figure S1: Efficacy controls for inhibition of Wnt and BMP signalling In situ hybridisations on E13.5 palatal shelf explants for Wnt target gene Lef1 and BMP target gene Id1, cultured for 24 hrs in the small molecule inhibitor IWP-2 and dorsomorphin respectively. Contralateral shelves shown as vehicle controls. Well known domains of target gene expression in palatal region are lost upon inhibitor treatment; see loss of strong Lef1 expression in tooth upon IWP-2 treatment, and loss of strong Id1 staining at medial palate edge (see arrows). Darker regions in inhibitor treated specimens represent background staining in areas of thickened tissue. Anterior to the right, medial up. Scalebar = 200 µm.

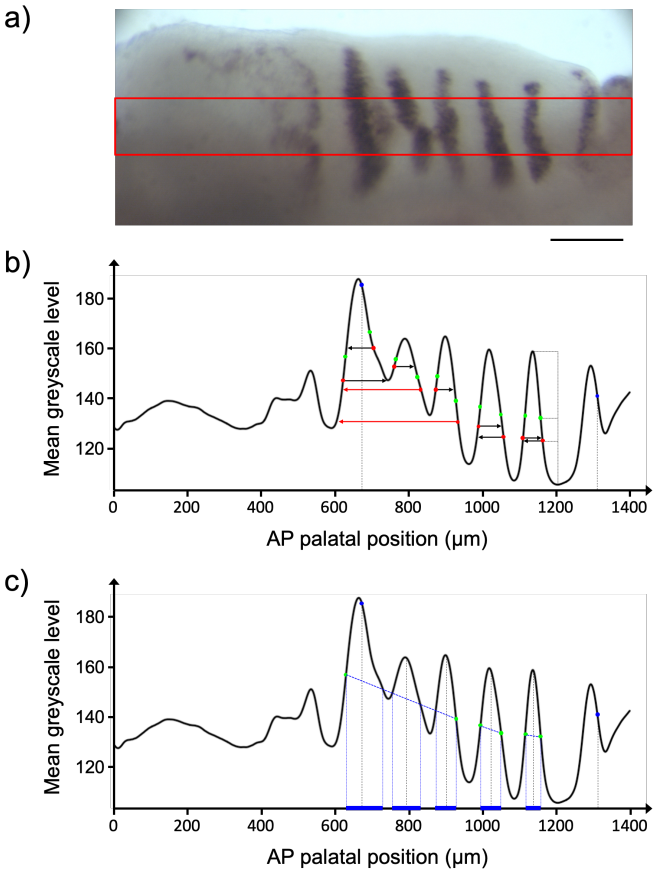

Figure S2: Identifying rugae from *Shh* in situ hybridisation of whole mount explant cultures

a) *Shh* in situ hybridisations on E13.5 palatal shelf explants cultured for 24 hrs. Red rectangle shows 150 µm band along which *Shh* staining intensity was measured. Anterior to right, medial up. Scalebar = 200 µm.

b) Plot of mean *Shh* staining intensity for each AP position along the red rectangle in a), against the AP position relative to the posterior of the image. Blue dots and coarse dashed lines denote positions of ruga 8 and ruga 1, identified manually on specimen in a). Green and red dots denote half heights and one third heights respectively for each peak, as illustrated by fine dashed lines on anterior of ruga 2. Arrows denote the next position in the array with the same intensity as marked by the red dots, with red arrows identifying potentially fused rugae.

c) Plot of mean *Shh* staining intensity as in b) with blue bars denoting the positions of the rugae, with anterior and posterior boundaries determined by the blue dashed lines. Black dashed lines denote position of rugae, taken as the manually identified positions for ruga 8 and ruga 1, and the ruga midpoints for the remaining rugae.

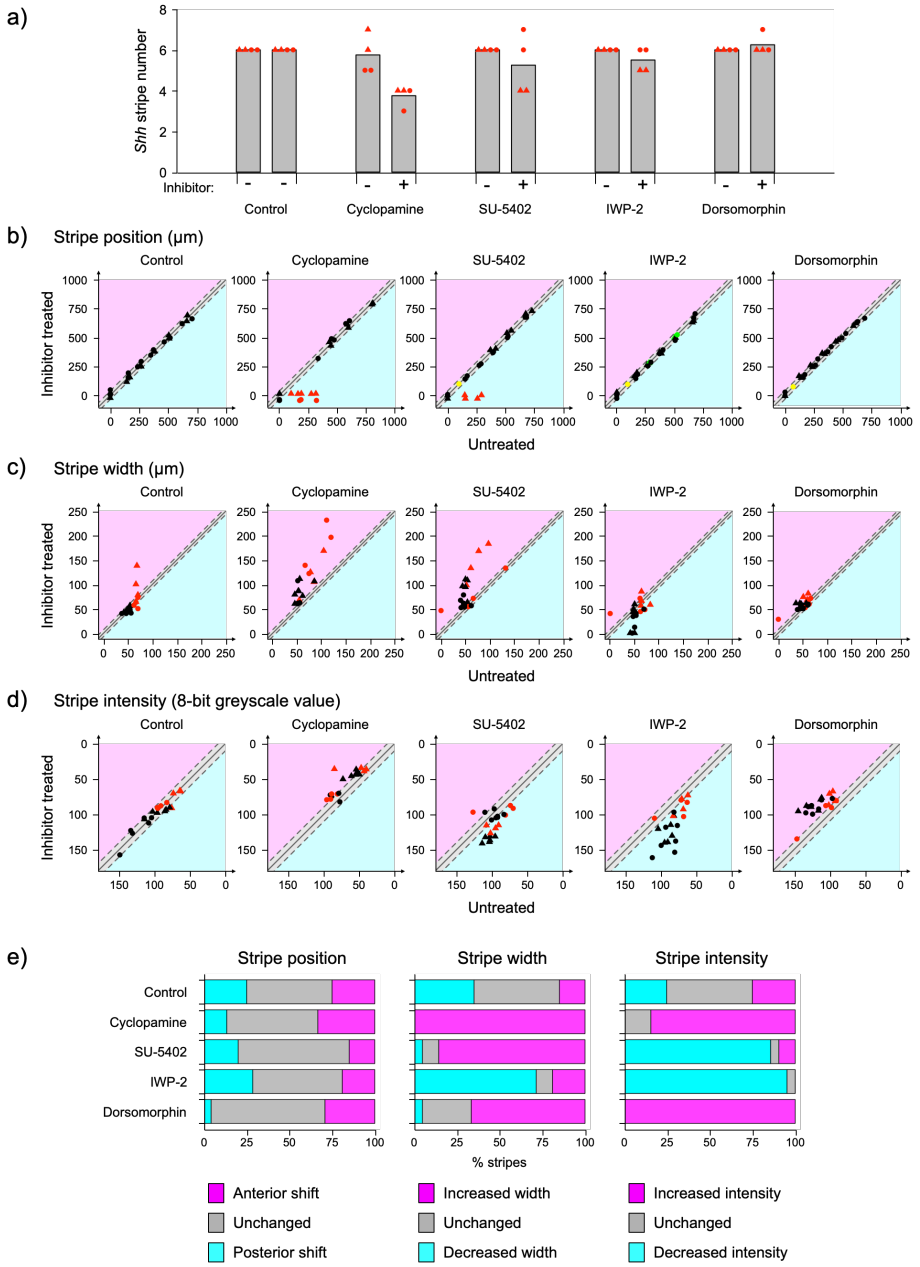

Figure S3: Effects of pathway inhibition on the pattern of the rugae

a) Mean number of rugae as marked by clear peaks of *Shh* expression in E13.5 palatal shelves cultured for 24 hrs with the specified inhibitor (+) or vehicle (-).

b-d) Plots of *Shh* stripe position b), width c) and stripe intensity d) for all ruga from explants for specified inhibitor treatment, plotted against values for the equivalent ruga in stage matched untreated (vehicle) control (see Methods for details of quantifications). Plots from paired untreated explants are also shown to show levels of variability in the absence of inhibitor. Solid grey lines denote equal values, dashed lines represent one median displacement around the line of equal values for untreated explants (see Methods for details). Magenta regions represent larger, and cyan regions smaller, values in inhibitor treated explants. For stripe position b), red points relate to rugae determined to have fused with another ruga in the inhibitor treated explants, with their position in plotted against the position of that ruga in the inhibitor treated explant. Yellow and green points relate to rugae in the inhibitor treated and untreated explants respectively, where the equivalent ruga could not be identified in the stage matched explant (respectively the untreated or inhibitor treated). For measures of stripe width c) and intensity d) points in red denote posterior rugae (see Methods).

e) Percentage of rugae for each treatment lying within one median displacement from the line of equal values (grey), or above (magenta) and below (cyan), for each of the three measures in b-d).

All plots depict quantifications from four pairs of explants. Drug treatments were carried out at the doses specified in the Methods, plus an additional dose, with points pertaining to lower doses shown as circles and higher dose as triangles in all plots. Doses used are: cyclopamine 20 µM and 80 µM, SU-5402 40 µM and 80 µM, IWP-2 10 µM and 50 µM, dorsomorphin 10 µM and 50 µM.

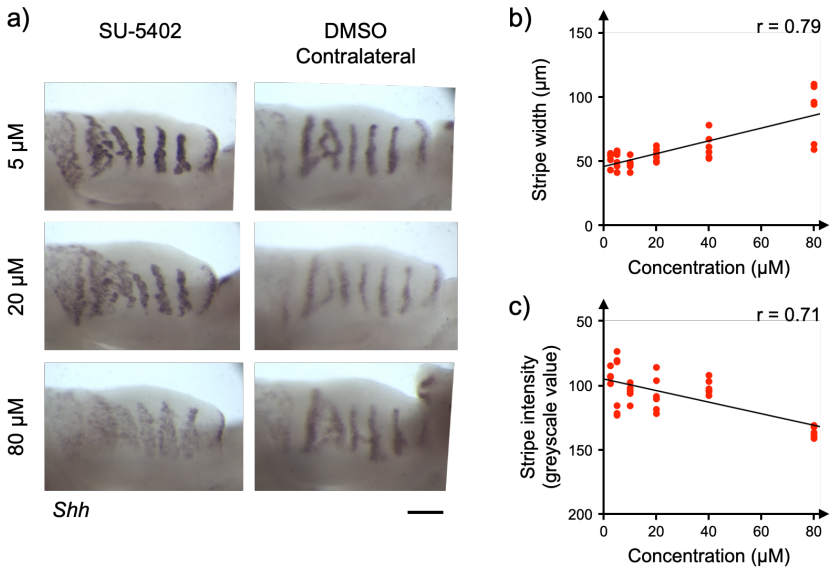

Figure S4: Titration of FGF inhibitor SU-5402

a) *Shh* expression in palatal shelves explanted at E13.5 and cultured with the FGF receptor inhibitor SU-5402 for 24 hrs at the indicated doses, alongside the contralateral shelves which were cultured in DMSO.
Scalebar = 200 µm.
b) Plot showing positive correlation between concentration of SU-5402 and *Shh* stripe width.
c) Plot showing positive correlation between concentration of SU-5402 and *Shh* stripe greyscale intensity. Note that as more intense staining has a lower greyscale value, greyscale axis is plotted in reverse to show a decrease in staining intensity with increased concentration of inhibitor.
Points in b) and c) depict ruga 4 to 2 from two embryos per concentration. Other rugae are not plotted as measurements were not calculated for ruga 1 (see methods), while more posterior rugae appear very variable even in control treatments (see Results). Pearson's product-moment correlation coefficient (r) is given for each plot in b) and c).

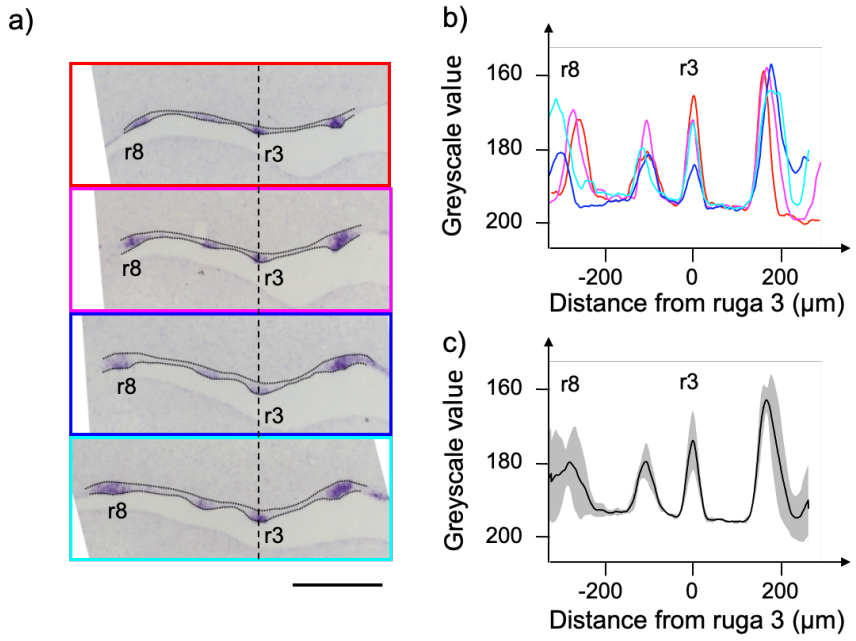

Figure S5: Quantification of striped rugal expression

a) In situ hybridisation showing Shh expression in sagittal sections taken at 35 µm increments across a E13.5 palatal shelf, ordered from medial most (red outline) to lateral most (cyan outline). The positions of ruga 3 and ruga 8 are indicated. Dotted lines illustrate the extent of the palatal epithelium used for quantifications. Anterior to right.
Scalebar = 200 µm.
b) Intensity profiles for each section aligned by the position of ruga 3. Peaks in Shh intensity at ruga 3 and ruga 8 are indicated. Profiles coloured as in a).
c) Mean intensity profile from the four sections in a) and b). Shaded area represents 1 +/-sd.

Figure S6: Additional pathway marker quantification

In situ hybridisation of sagittal section through E13.5 palatal shelf for additional markers of pathway activity. Dotted lines illustrate the extent of the palatal epithelium and the underlying mesenchyme used for quantifications. Anterior to right. The intensity profile averaged across the palatal shelf shown for each specimen from which illustrated in situ is taken for gene of interest (coloured trace) and *Shh* (grey trace) for the epithelium and mesenchyme. Shaded areas represent 1 sd around gene of interest (for clarity of presentation, variation around *Shh* trace is not shown). For each marker, the number of specimens showing the observed pattern are: *Ptc1* 41, *Erm* 38, *Spry2* 36 and *Axin2* 43. Scalebars = 200 µm.

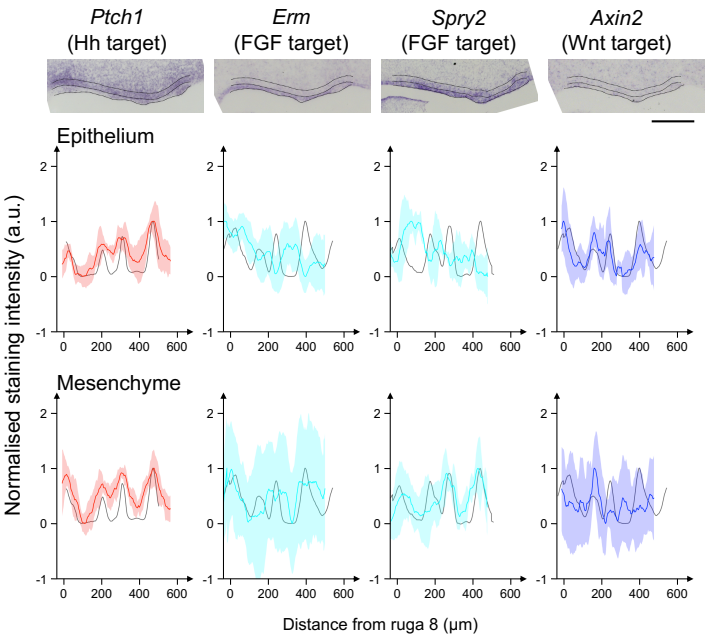

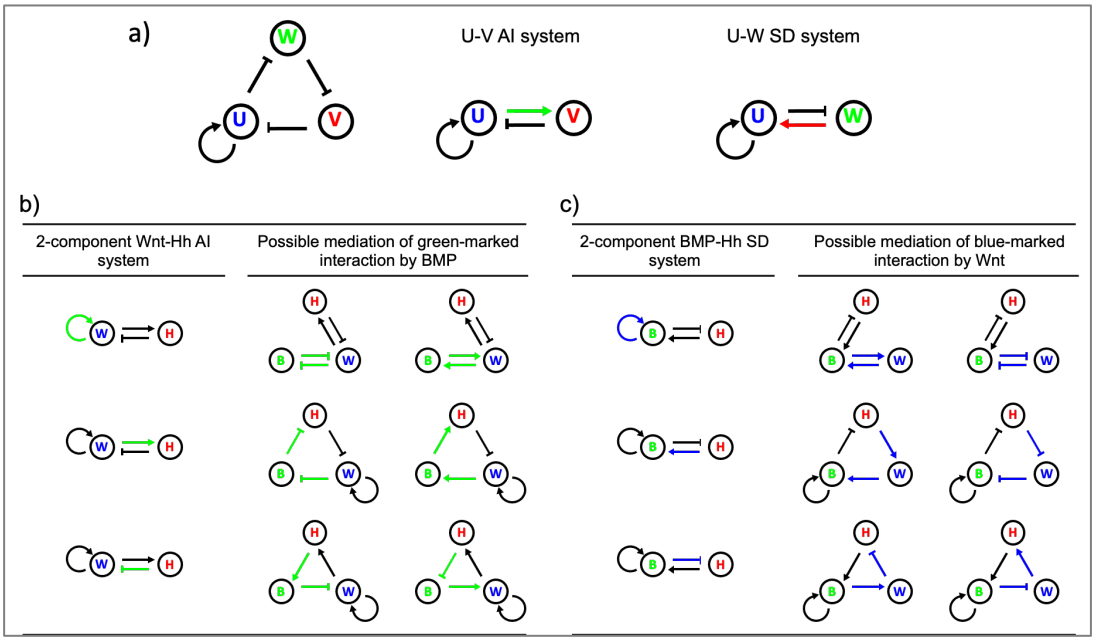

Figure S7: Adding a component as a mediator of an interaction

a) Network topology comprising three components U, V and W. This topology can be interpreted as a two-component activator-inhibitor system between 'master morphogens' U and V, where the positive interaction from U to V is 'mediated' by a double inhibition (ie a positive interaction) through W (see green arrow in U-V AI system). Alternatively, this same three-component topology can be interpreted in a similar manner as a substrate -depletion system with 'master morphogens' U and W, where V 'mediates' the positive interaction from W to U (see red arrow in U-W SD system).

b) All possible ways that an interaction in a two-component Wnt-Hh AI network (marked in green) can be 'mediated' by BMP in the adjacent three-component Wnt-BMP-Hh RD networks. Interaction in the three-component RD networks maintain the net sign of the marker interactions in the two-component networks; the phase of BMP relative to Wnt and Hh is not considered.

c) Same as in b) for Wnt mediating interaction in a two-component BMP-Hh SD network (with interactions 'mediated' by Wnt in blue).

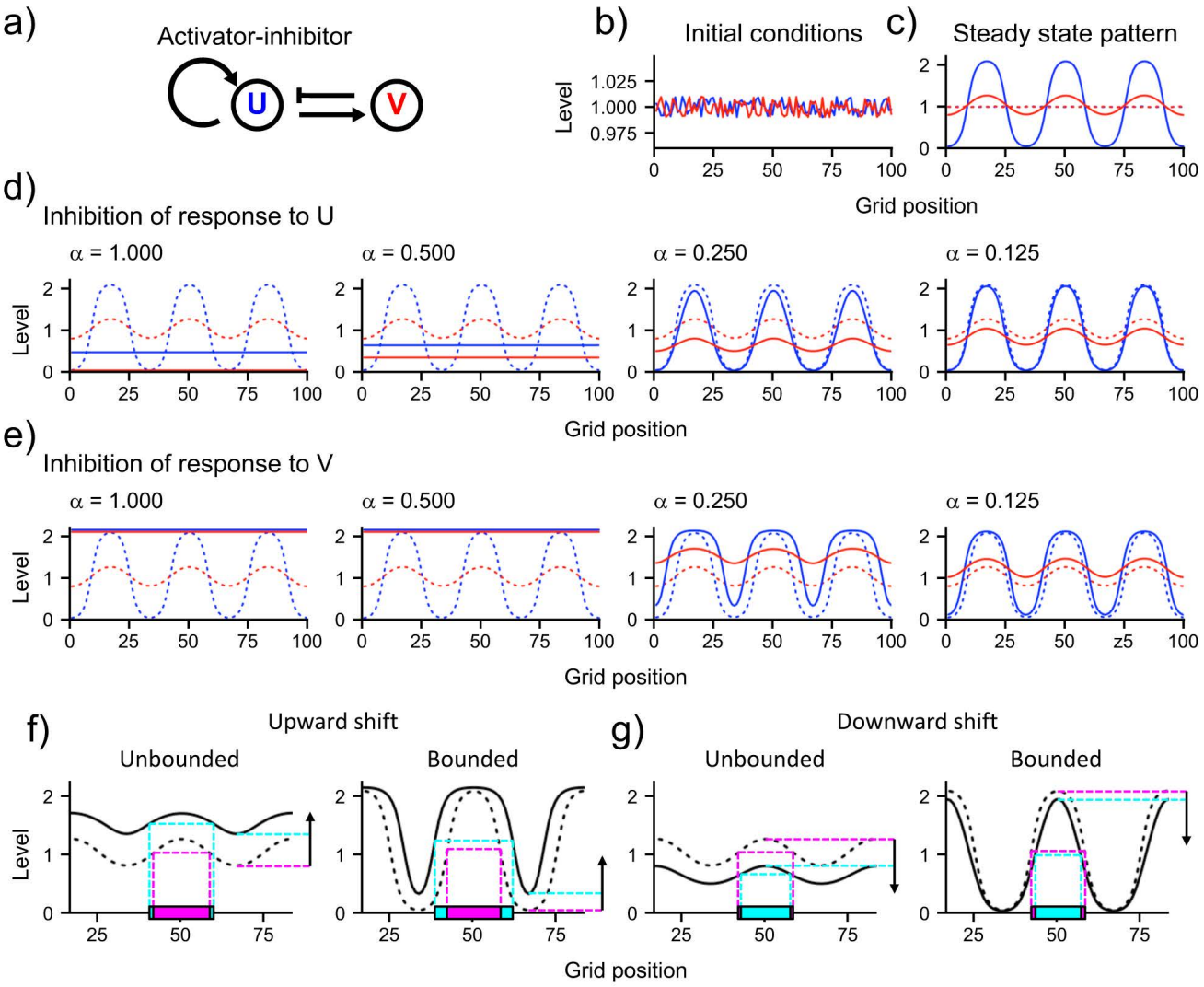

Figure S8: Illustrative simulation of two-component reaction-diffusion system show response of waves to inhibition of components

a) Two-component activator-inhibitor topology used for illustrative simulations. Simulations carried out as detailed in methods with u_1 is component U and u_2 is component V, with a_{11} = 0.017, a_{12} = -0.013, a_{21} = 0.016, a_{22} = 0.000, b_1 = 0.005, b_2 = 0.001, c_1 = 0.009, c_2 = 0.016, $fmax_1$ = 0.019, $fmax_2$ = 0.035, D_1 = 0.63 and D_2 = 24.17.

b) Illustration of initial conditions of U and V as described in Methods.

c) Steady state pattern of waves of U and V after simulation from the initial conditions in b). Initial conditions also shown as dashed lines (note difference in scale between b) and c).

d-e) Effect on steady state waves in c) of subsequent inhibition of response to U and V respectively for decreasing strengths of inhibition (values of α – see Methods). For comparison dashed lines show waves of U and V in the absence of inhibition. For b-e) component U is shown in blue, and component V in red.

f-g) Illustrative examples of the effects of inhibitions on waves, with solid waves showing shape after inhibition and dashed waves the uninhibited shape. Waves can shift up (as in f), either in an unbounded or bounded manner. In the latter case only troughs noticeably shift upwards with little effect on the position of peaks (see arrows to the right of plots showing difference in positions of inhibited (cyan) and uninhibited (magenta) troughs. Alternatively, waves can shift down (as in g), either in an unbounded or bounded manner. In the latter case only peaks noticeably shift downwards with little effect on the position of troughs (see arrows to the right of plots showing difference in positions of inhibited (cyan) and uninhibited (magenta) peak. The bounded condition in particular, can show a change in wave width, with an increase when the wave shifts up (see f) and a decrease when it shifts down (see g) as determined by the width of a wave taken at half the height from trough to peak (see dashed cyan (for inhibited) and magenta (for uninhibited) lines and bars).

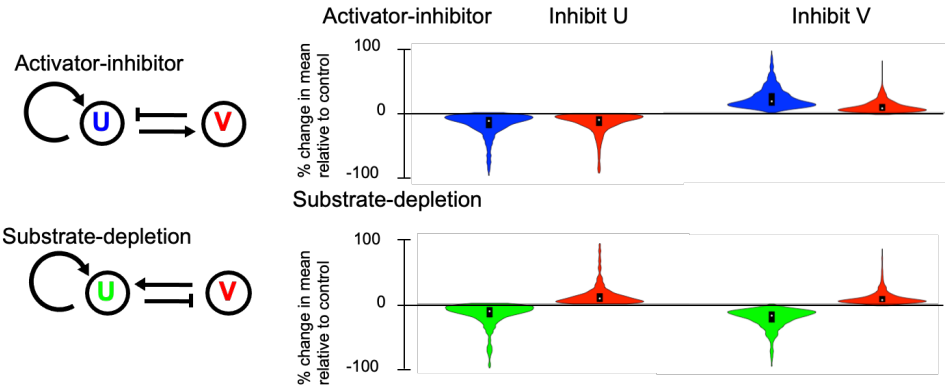

Figure S9: Inhibition of production produces the same outcomes as inhibition of response
Violin plots showing percentage change in the mean level of components U and V in illustrated activator-inhibitor (AI) and substrate-depletion (SD) RD networks, on inhibition of the production of component U and V in RD simulations.

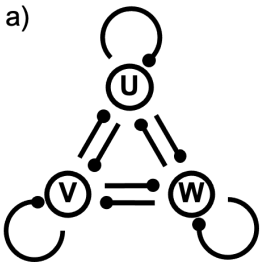

b)

All possible topologies:	**19683**
Degradation by default:	**5832**
Stable DDI topologies:	**1492**
Strongly connected:	**1396**
For each phase relationship:	**498**
Minimal topologies (per phase):	**45**

Figure S10: Three-component topologies and exclusion by successive constraints
a) Three-component network topology showing the nine possible interactions captured in the reaction matrix.
b) Enumeration of topologies recovered from parameter search under different constraints as detailed in text.

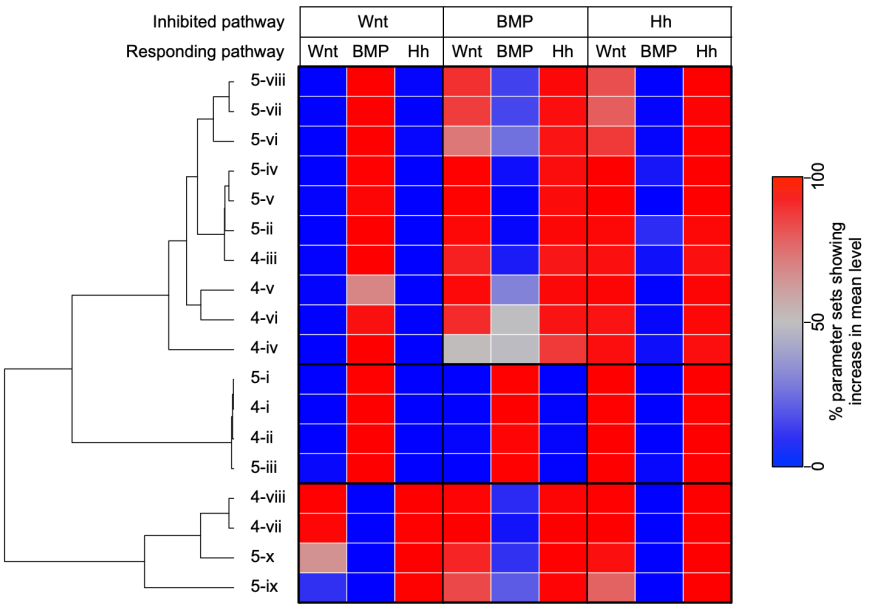

Figure S11: Responses of three-component networks to perturbation
Full heat map showing the percentage of parameter sets where the level of each component increases in response to the inhibition of each component in the network in RD simulations. Topology names are as in figure 3. Hierarchical clustering shows that the behaviours of the topologies fall into the main categories for which all three components show similar behaviour.

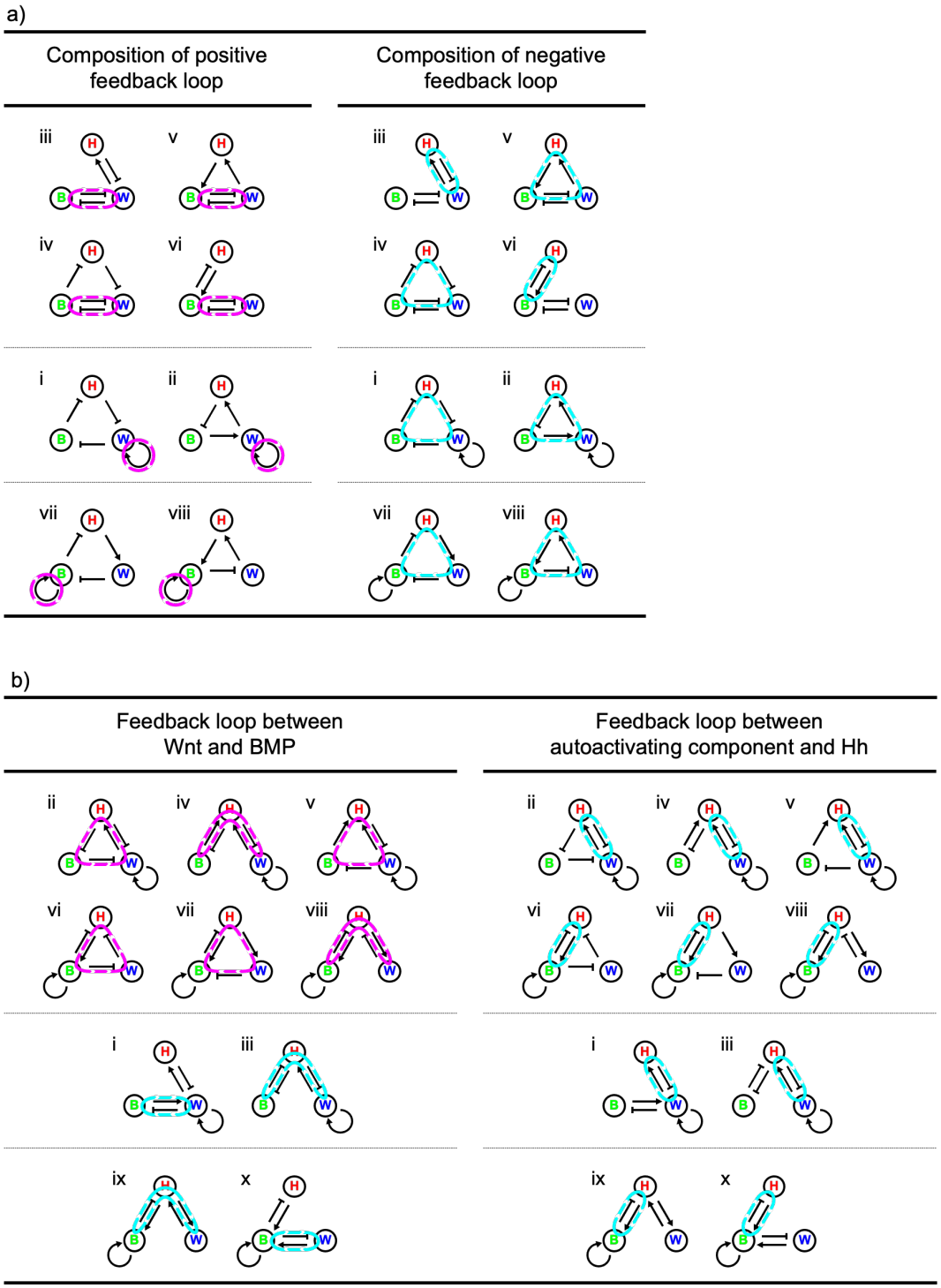

Figure S12: Feedback loops in three-component networks

a) Schematics showing the eight minimal 4-interaction RD networks recovered from the parameter search, with either the single positive feedback loop marked in magenta (left) or the single negative feedback loop marked in cyan (right). Topologies are group as according the the hierarchical clustering in figure S7.

b) Schematics showing the ten minimal 5-interaction topologies networks recovered from the parameter search. On left, the net feedback between Wnt and BMP is marked, with magenta for a positive feedback, or cyan for a negative feedback. (It should be noted that for some topologies (such as iv, vii, iii and ix) the feedback is indirect with both the interaction from Wnt to BMP and BMP to Wnt pass through Hh. For example, in iv, while there is no single positive feedback loop, the net interaction between Wnt and BMP is a mutual inhibition and therefore a net positive feedback.) On the right, the presence of a negative feedback between Hh and the autoactivating component (Wnt or BMP) is marked in cyan. Topologies are group as according the the hierarchical clustering in figure S7.

Wnt in blue, BMP in green and Hh in red.

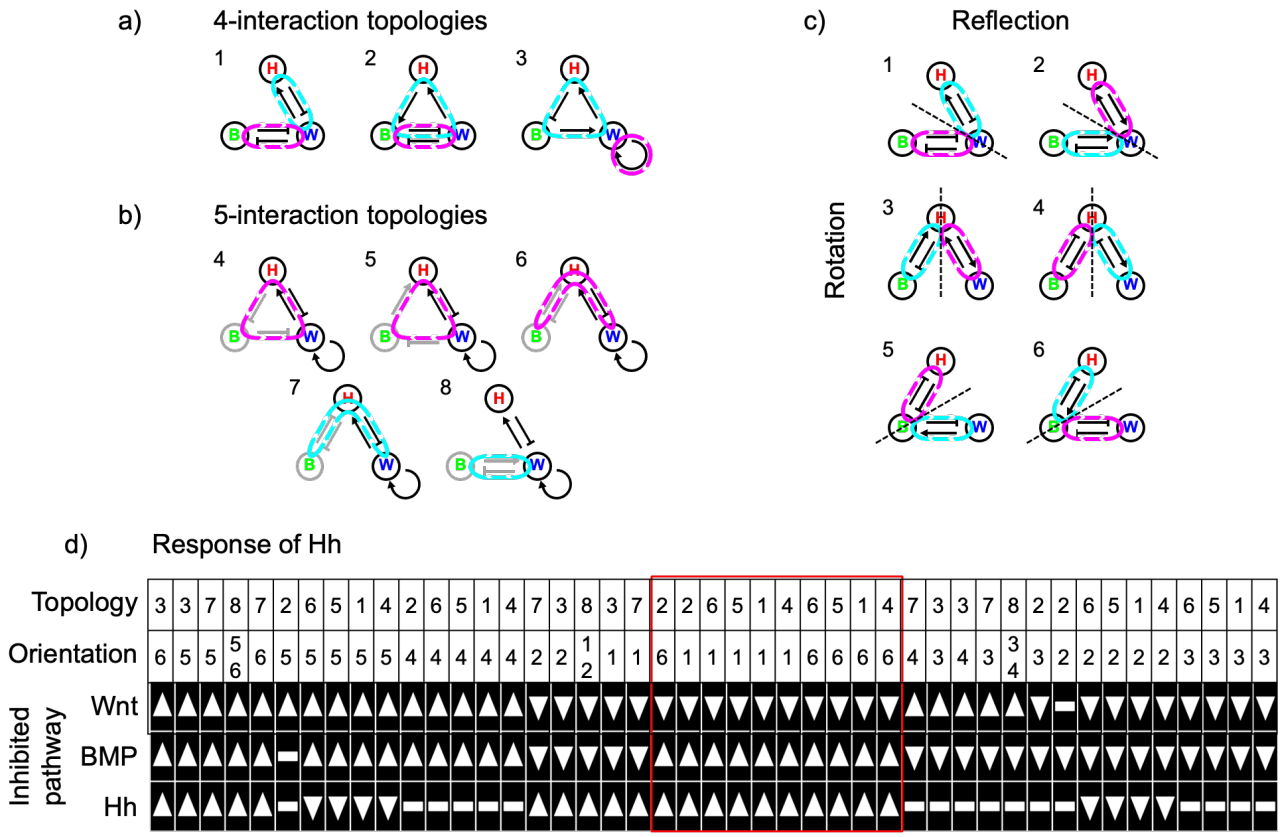

Figure S13: Using topology to constrain the response to perturbation of minimal three-component networks

a) Illustrative examples of minimal 4-interaction three-component RD networks showing the three different ways a single positive and negative feedback loop can be combined. The positive feedback loop can pass through one (topology 3) or two (topologies 1 and 2) components, and the negative feedback can pass through two (topology 1) or three (topologies 2 and 3) components. Positive feedback loops in magenta, negative feedback loops in cyan.

b) Illustrative examples of 5-interaction three-component RD networks showing the five different ways that an external component can be wired into a two-component RD core, such that the new topology is not an elaboration of one of the minimal architectures in a). Core components and interactions in black, with external in grey. The nature of the net feedback between the external component (BMP in the illustrative examples) and the core positive feedback component (Wnt in the illustrative examples) is shown as a magenta loop for positive feedback and a cyan loop for negative feedback.

c) Examples of three-component RD networks showing the six different orientations that a set of 3-component RD loops can take, using the 4-interaction minimal architecture in a) 1 as an illustrative example. The feedback loops can be rotated into three different orientations (1, 3 and 5), as shown by the positions of the two feedback loops relative to the dashed black line. In each orientation, the architectures can be reflected around the dashed black line to give a further three orientations (2,4 and 6).

d) Response of Hh to inhibition of Wnt, BMP and Hh for all 45 possible minimal three-component Wnt-BMP-Hh topologies based on reaction term analysis. Topologies are specified by the combination of a topology (1 to 8 from a) and b)) and an orientation (1 to 6 from c)). Topology architecture 8 is symmetrical upon reflection and therefore two the topology under two possible orientations is the same. The direction of response of Hh shown by arrowhead, with up arrow indicating increase and down arrow decrease. Where the response is unconstrained a white bar is shown. Coupling between components (see supplementary note 4 and figure 4) is not shown. The ten topologies for which the predicted responses are consistent with experimental observations are marked in red. These are the same topologies as recovered by the RD analysis (see figure 3).

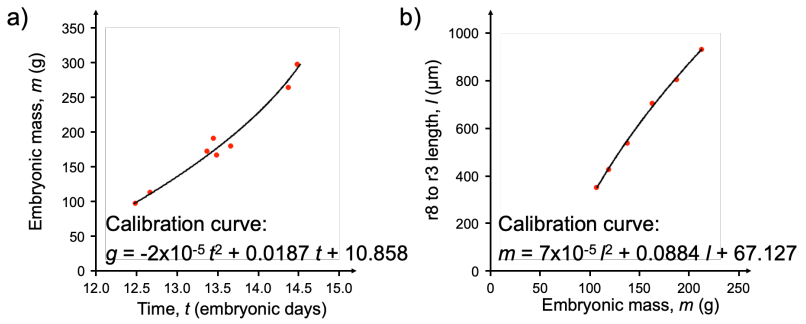

Figure S14: Calibration curves for converting palatal length into time
a) Plot of time litters of mice were collected vs. the mean embryo mass for that time (n = 3 litters per time point).
b) Plot of embryonic mass (taken as the midpoint of the bin) against average ruga 3 to ruga 8 length the the weight bin.
For a) and b), equations of best fit quadratics are given which allowing the conversion of palatal lengths to time in embryonic days.

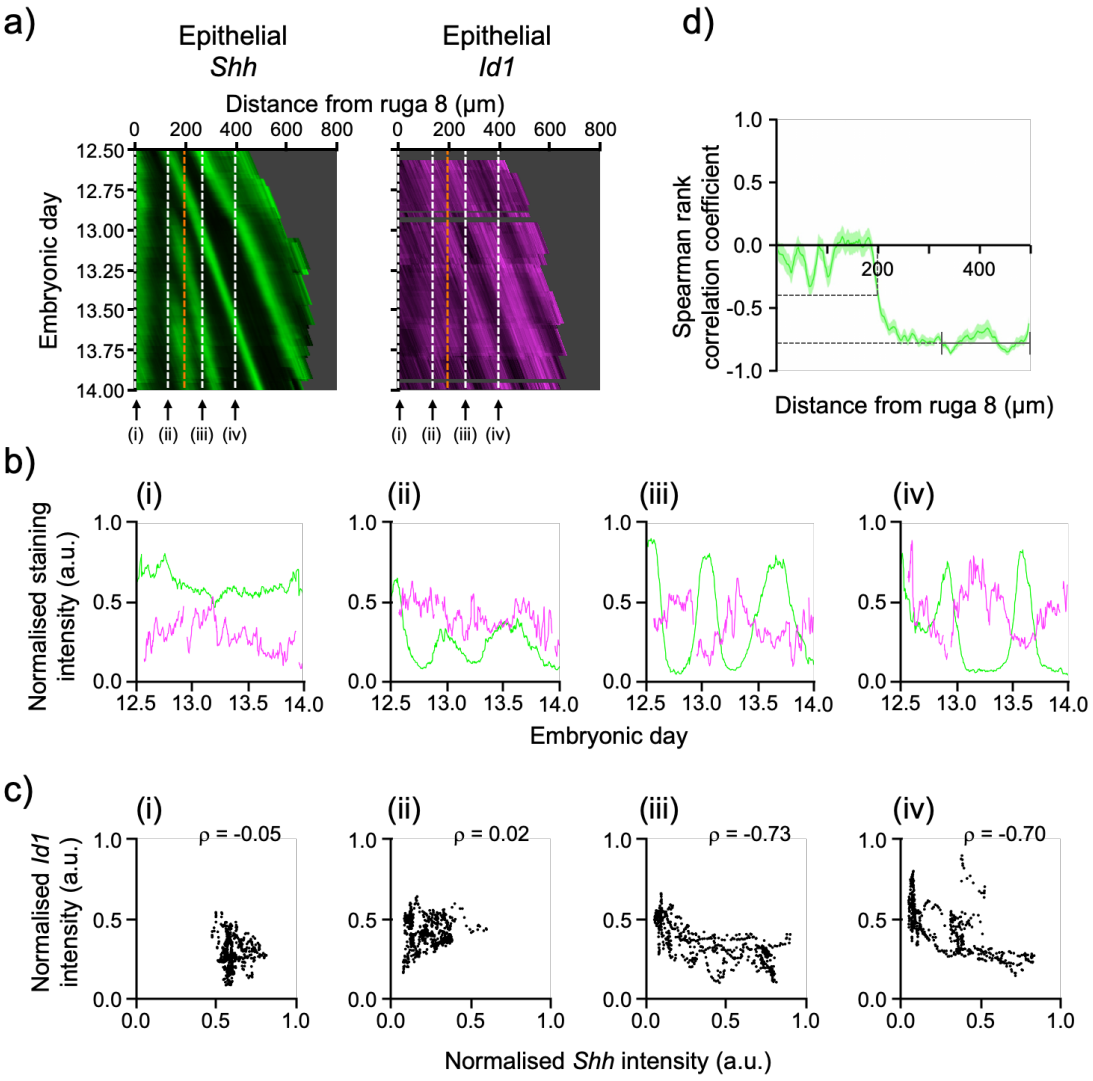

Figure S15: Illustrative example of how the appearance of periodic target gene expression relative to the onset of rugal *Shh* expression is identified
a) Kymographs of epithelial Shh (green) and epithelial Id1 (magenta) as in figure 6a.
b) Plots of normalised staining intensity for *Shh* (green) and Id1 (magenta) against time in embryonic days at four different distances from ruga 8 (i-iv), as marked by arrows and white dashed lines in a).
c) Plots of normalised staining intensity for *Shh* against Id1 for 600 equal time steps from 12.5 to 14.0 embryonic days at four different distances from ruga 8 (i-iv), as in b). The Spearman rank correlation coefficient (ρ) is given for each distance.
d) Plot of Spearman rank correlation coefficient (ρ) against distance from ruga 8 for Id1. Shaded area represents 95 % confidence interval from bootstrapping (see Methods). Solid line represents mean correlation coefficient calculate over anterior third of palatal tissue. Dashed lines demonstrate how the position relative to ruga 8 where half this value is reached is used to determine the onset of out-of-phase Id1 expression, marked by orange dashed lines in a).

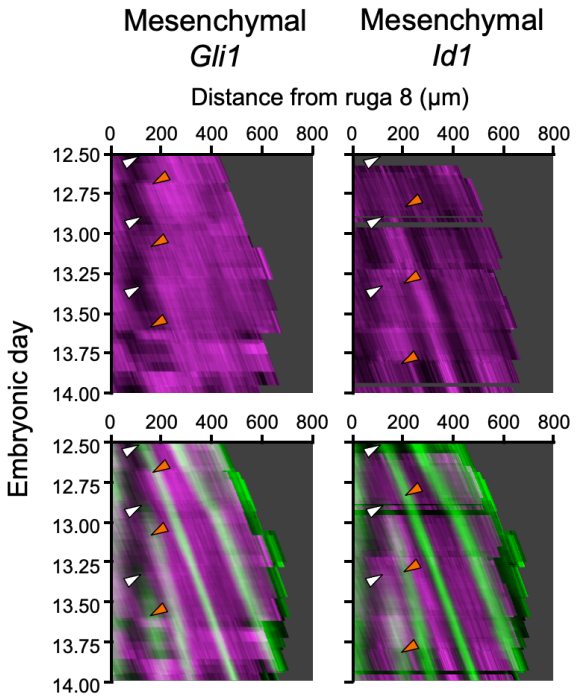

Figure S16: Kymographs showing patterns of mesenchymal expression through time for *Gli1* and *Id1*
Kymographs showing the pattern of expression of mesenchymal *Gli1* and *Id1* through time (magenta) and their expression relative to *Shh* (green) for rugae 3, 4 and 5. White arrowheads indicate the approximate onset of *Shh* expression for each ruga, and orange arrowheads indicate approximate positions of the change in the expression pattern of each target gene associated with each ruga.

Supplementary Tables:

Topology	Steady state (%)	Maintain wave number (%)	Shift in wave position (%)			
			Inhibit U		Inhibit V	
			U	V	U	V
AI (R)	95.2	100.0	99.8	100.0	100.0	100.0
SD (R)	89.6	100.0	99.6	100.0	99.9	100.0
AI (P)	95.2	100.0	99.9	100.0	99.4	100.0
SD (P)	89.5	100.0	99.8	100.0	100.0	100.0

Table S1: Behaviour of simulations for two-component RD topologies.
Table showing for each topology what percentage of 1000 randomly generated parameter sets consistent with the criteria for DDI reached a steady state after 1000 time steps, and what percentage of these maintained their wave number after inhibition (there is no change or loss of periodicity). For parameter sets maintaining wave number, the proportion of waves showing a shift in position (either upwards or downwards – see Methods) is given for both components of the inhibition of each component. For the two two-component network topologies activator-inhibitor (AI) and substrate-depletion (SD) both the inhibition of the response to each component (R) and the inhibition of their production (P) were considered.

Topology	Steady state (%)	Maintain wave number (%)	Shift in wave position (%)								
			Inhibit W			Inhibit B			Inhibit H		
			W	B	H	W	B	H	W	B	H
4-i	85.5	99.8	99.6	99.8	100.0	99.8	100.0	99.9	100.0	100.0	100.0
4-ii	93.2	99.7	99.9	100.0	100.0	99.9	100.0	100.0	99.9	100.0	99.9
4-iii	80.1	99.1	99.7	99.9	99.9	100.0	99.7	100.0	94.0	99.5	99.9
4-iv	89.5	98.0	99.9	99.9	100.0	99.8	99.5	100.0	90.5	99.7	100.0
4-v	92.5	99.9	100.0	85.9	100.0	100.0	82.9	100.0	98.6	95.4	99.8
4-vi	83.9	99.9	99.8	85.9	100.0	99.8	86.6	100.0	98.0	94.9	99.9
4-vii	82.6	100.0	99.4	99.9	100.0	100.0	99.8	100.0	100.0	100.0	100.0
4-viii	82.6	100.0	94.9	99.9	100.0	99.5	99.8	100.0	99.3	99.9	100.0
5-i	92.7	99.9	100.0	100.0	100.0	99.6	99.8	100.0	99.9	100.0	99.9
5-ii	90.5	99.9	99.7	100.0	100.0	99.7	99.9	100.0	99.8	99.8	99.9
5-iii	94.3	100.0	99.8	100.0	100.0	99.8	100.0	100.0	99.7	100.0	100.0
5-iv	92.7	100.0	100.0	100.0	100.0	99.7	99.4	99.4	99.7	99.9	100.0
5-v	94.6	100.0	99.8	99.9	100.0	99.6	99.8	99.0	99.5	99.8	100.0
5-vi	86.4	99.9	100.0	99.3	99.0	99.4	99.7	100.0	93.6	99.5	99.9
5-vii	73.1	99.9	100.0	99.6	100.0	100.0	99.6	100.0	99.7	99.7	99.7
5-viii	92.0	100.0	98.7	99.5	99.9	99.6	99.5	99.8	97.3	99.6	99.7
5-ix	80.6	100.0	100.0	99.0	99.9	100.0	99.8	100.0	99.8	99.6	100.0
5-x	87.0	99.7	99.5	99.0	99.4	99.7	99.6	100.0	99.7	99.7	100.0

Table S2: Behaviour of simulations for three-component RD topologies.
Table showing for each topology (as defined in figure 3b) the behavior of RD simulation of the three components Wnt (W), BMP (B) and Hh (H), as detailed in supplementary table S1. As stated in Methods, for Wnt inhibition is at the level of production, while for BMP and Hh inhibition is at the level of response.

Appendix S1. Supplementary Notes for Economou et al. " Perturbation analysis of a multi-morphogen Turing Reaction-Diffusion stripe patterning system reveals key regulatory interactions"

1: Review of Conditions for DDI in 2- 3- and *N*-component systems

The conditions for a diffusion driven instability (DDI) have been extensively analysed. For completeness, we present general conditions for a DDI, as well as specific criteria for assessing whether specific parameterisations of two- and three-component RD systems will give a DDI.

1.1: General conditions for a DDI

We considered a general reaction-diffusion system of the form

$$\frac{\partial \boldsymbol{u}}{\partial t} = \boldsymbol{f}(\boldsymbol{u}) + \boldsymbol{D}\nabla^2\boldsymbol{u},$$

where $\boldsymbol{u}$ is a vector of N reactant concentrations and $\boldsymbol{D}$ is a diagonal $N\times N$ matrix of diffusion coefficients where $N \geq 2$, such that

$$\boldsymbol{u} = \begin{pmatrix} u_1 \\ u_2 \\ \vdots \\ u_N \end{pmatrix} \text{ and } \boldsymbol{D} = \begin{pmatrix} D_1 & 0 & \cdots & 0 \\ 0 & D_2 & \cdots & 0 \\ \vdots & \vdots & \ddots & \vdots \\ 0 & 0 & \cdots & D_N \end{pmatrix}.$$

Following the well-established linear stability approach to deriving conditions for DDI, as outlined Murray (2003) (see also White and Gilligan 1998, Marcon et al. 2016) (N.B. References below), we derive the stability matrix $\boldsymbol{S}$, for which

$$\boldsymbol{S} = \boldsymbol{J} - \boldsymbol{D}q^2,$$

where q is the wave number of a spatially-periodic perturbation, and $\boldsymbol{J}$ is the Jacobian matrix of the reaction system, where the elements J_{ij} are the first partial derivatives of the components of $\boldsymbol{f}$, evaluated at a spatially-uniform steady state, such that

$$\boldsymbol{J} = \begin{pmatrix} J_{11} & J_{12} & \cdots & J_{1N} \\ J_{21} & J_{22} & \cdots & J_{2N} \\ \vdots & \vdots & \ddots & \vdots \\ J_{N1} & J_{N2} & \cdots & J_{NN} \end{pmatrix}, \quad J_{ij} = \frac{\partial f_i(u_1,u_2,\ldots,u_N)}{\partial u_j}.$$

Solving the system

$$\det[\lambda \boldsymbol{I} - \boldsymbol{S}] = 0$$

gives the dispersion relation for the eigenvalues λ of $\boldsymbol{S}$:

$$\lambda^N + a_1(q^2)\lambda^{N-1} + a_2(q^2)\lambda^{N-2} + \cdots + a_N(q^2) = 0.$$

For diffusion driven instability, the system must be stable without diffusion and unstable with diffusion. Thus, when q=0, all solutions λ of the dispersion relation must have negative real part, and there must exist positive values of q^2 for which there is at least one solution λ with positive real part.

We will now consider the specific cases of two- and three-component RD systems.

1.2: Two-component system

For a two-component system of the form above, the dispersion relationship takes the form

$$\lambda^2 + a_1(q^2)\lambda + a_2(q^2) = 0,$$

with coefficients

$$a_1(q^2) = -(J_{11} + J_{22}) + q^2(D_1 + D_2),$$

$$a_2(q^2) = (J_{11}J_{22} - J_{12}J_{21}) - q^2(J_{11}D_2 + J_{22}D_1).$$

Following the approach of Murray (2003) gives the conditions for a DDI. Stability in the absence of diffusion requires

$$J_{11} + J_{22} < 0,$$

and

$J_{11}J_{22} - J_{12}J_{21} > 0,$

and instability with diffusion requires

$J_{11}D_2 + J_{22}D_1 > 2\sqrt{D_1D_2(J_{11}J_{22} - J_{12}J_{21})} > 0.$

As is well established (see Murray 2003), if J_{11}>0 and J_{22}<0, the two components will be in-phase when J_{12}<0 and J_{21}>0, and out-of-phase when J_{12}>0 and J_{21}<0.

1.3: Three-component system

For a three-component system of the form above, the dispersal relationship takes the form

$\lambda^3 + a_1(q^2)\lambda^2 + a_2(q^2)\lambda + a_3(q^2) = 0,$

with coefficients

$a_1(q^2) = -(J_{11} + J_{22} + J_{33}) + q^2(D_1 + D_2 + D_3),$

$a_2(q^2) = (J_{11}J_{22} - J_{12}J_{21} + J_{11}J_{33} - J_{13}J_{31} + J_{22}J_{33} - J_{23}J_{32}) - q^2(J_1D_2 + J_1D_3 + J_2D_1 + J_2D_3 + J_3D_1 + J_3D_2) + q^4(D_1D_2 + D_1D_3 + D_2D_3),$

$a_3(q^2) = -(J_{11}J_{22}J_{33} + J_{12}J_{23}J_{31} + J_{13}J_{32}J_{21} - J_{11}J_{23}J_{32} - J_{22}J_{13}J_{31} - J_{33}J_{12}J_{21}) + q^2((J_{11}J_{22} - J_{12}J_{21})D_3 + (J_{11}J_{33} - J_{13}J_{31})D_2 + (J_{22}J_{33} - J_{23}J_{32})D_1) - q^4(J_{11}D_2D_3 + J_{22}D_1D_3 + J_{33}D_1D_2) + q^6D_1D_2D_3.$

Following the approach of White and Gilligan (1998), we considered the Routh-Hurwitz criteria. Stability without diffusion requires

$a_1(0) > 0 \ \wedge \ a_3(0) > 0 \ \wedge \ a_1(0)a_2(0) - a_3(0) > 0$

and instability with diffusion requires

$a_1(q^2) < 0 \ \vee \ a_3(q^2) < 0 \ \vee \ a_1(q^2)a_2(q^2) - a_3(q^2) < 0.$

As detailed by White and Gilligan (1998), the conditions for instability can only be satisfied if

$$a_3(q^2) < 0$$

or

$$a_1(q^2)a_2(q^2) - a_3(q^2) < 0.$$

Both of the functions in the inequalities are cubic functions of the form

$$y(q^2) = a(q^2)^3 + b(q^2)^2 + c(q^2) + d,$$

where a, b, c and d are constant coefficients. A DDI will occur if there exists a minimum turning point q_{TP}^2, for which $q_{TP}^2 > 0$, and $y(q_{TP}^2) < 0$ (see White and Gilligan (1998) for details).

RD systems with more than two components can destabilise either as monotonically growing spatially periodic patterns (as for two component systems) or temporally oscillating patterns. When the system is destabilized with real positive λ, the spatial patterns grow monotonically, while if λ has non-zero imaginary parts, they will oscillate temporally. White and Gilligan (1998) provide a detailed analysis of conditions for monotonically growing and oscillating patterns. From their analysis, a parameterization will be produce monotonically growing spatial patterns for all q^2 if

$$a_3(q^2) < 0,$$

$$a_1(q^2)a_2(q^2) - a_3(q^2) > 0,$$

and

$$a_1(q^2)^2 - a_2(q^2) > 0.$$

The function in the final condition is quadratic in q^2, with a minimum at q_{MIN}^2, such that $a_1(q_{MIN}^2)^2 - a_2(q_{MIN}^2) > 0$.

For each parameterization, a phase relationship was calculated as the eigenvector of the largest positive eigenvalue of the matrix

$$\boldsymbol{S} = \begin{pmatrix} J_{11} - D_1 q^2 & J_{12} & J_{13} \\ J_{21} & J_{22} - D_2 q^2 & J_{23} \\ J_{31} & J_{32} & J_{33} - D_3 q^2 \end{pmatrix},$$

calculated at the turning point q_{TP}^2 for which $a_3(q^2) < 0$. While this is not necessarily the phase pattern with which the pattern with the fastest growing wavelength will grow, it does give a phase pattern that is consistent with the network topology defined by the reaction matrix.

1.4: N-component system

For a general reaction diffusion system, Marcon et al. (2016) demonstrated that coefficients of the dispersion relationship, $a_k(q^2)$ for k =1,...,N, are of the form

$$a_k(q^2) = \sum_{\gamma_k \subseteq S_k^N} \left\{ (-1)^k \det[\boldsymbol{J}(\gamma_k)] + \sum_{m=1}^{k-1} q^{2(k-m)} \sum_{\gamma_m \subset \gamma_k} (-1)^m \det[\boldsymbol{J}(\gamma_m)] \det[\boldsymbol{D}(\tilde{\gamma}_m)] + q^{2k} \det[\boldsymbol{D}(\gamma_k)] \right\}, \quad (1.1)$$

where γ_k denotes a sequence of k distinct integers $\{i_1, \ldots, i_k\}$, where $1 \leq i_1 < i_2 < \cdots < i_k \leq N$ and S_k^N is the set of all possible sequences of k elements in $\{1, \ldots, N\}$, $\boldsymbol{J}(\gamma_k)$ denotes the $k \times k$ submatrix made up of coefficients with the column and row indices γ_k, and γ_m denotes a sequence of $m < k$ distinct integers, where $\gamma_m \subset \gamma_k$, and $\tilde{\gamma}_m$ is a complementary sequence of integers such that $\gamma_m \cap \tilde{\gamma}_m = 0$ and $\gamma_m \cup \tilde{\gamma}_m = \gamma_k$. As outlined in Marcon et al. (2016), there will be a single real and positive eigenvalue (and monotonically growing patterns will grow) if $a_k(q^2) > 0$ for $k < N$, and $a_N(q^2) < 0$.

2: Perturbation predictions from RD reaction terms

Our analysis of the response of RD systems to perturbations suggested that there is a relationship between the feedback loops within the RD system, and the nature of the response of the system to perturbation. Specifically, whether a component increases or decreases its level in response to the inhibition of another component depends on whether the components are in a positive or negative feedback loop. As the feedback loops are encoded by the reaction terms of the system, we considered what role the reaction terms could play in this behaviour. Preliminary simulations suggested that the response of an established spatially periodic steady state solution of an RD system to perturbation is predicted by the response of the reaction term equilibrium, and whether it increases or decreases in response to equivalent perturbations. We therefore decided to investigate further the factors that govern the responses of the reaction terms.

2.1: Shape of N-component response

We considered the response of a system of N components, using a system of linear ODEs equivalent to that used for the full reaction-diffusion system we used before, where

$$\frac{du_i}{dt} = \sum_{j=1}^{N} a_{ij}u_j + b_i - c_i u_i.$$

The parameters a_{ij} represent the weight of the interaction from component u_j to component u_i, where a positive term indicates an activation and a negative term an inhibition, b_i is a background production term and c_i is the linear degradation rate of component u_i.

The position of the equilibrium is given by setting $\frac{du_i}{dt} = 0$ for all i, and as in (Desoer 1960), rearranging this gives

$$u_i = (\boldsymbol{A}^{-1}\boldsymbol{b})_i = -\frac{\sum_{j=1}^{N} \mathrm{C}[\boldsymbol{A}]_{ji} b_j}{\det[\boldsymbol{A}]},$$

where the matrix $\boldsymbol{A}$ is given by

$$\boldsymbol{A} = \begin{pmatrix} a_{11} - c_1 & a_{12} & \cdots & a_{1N} \\ a_{21} & a_{22} - c_2 & \cdots & a_{2N} \\ \vdots & \vdots & \ddots & \vdots \\ a_{N1} & a_{N2} & \cdots & a_{NN} - c_N \end{pmatrix},$$

and $\mathrm{C}[\boldsymbol{A}]_{ji}$ is the cofactor of the element of the j^{th} row and i^{th} column of $\boldsymbol{A}$.

We considered the effect of inhibiting a component on the equilibrium levels of the system. Specifically, we looked at the effect of inhibiting component u_1 on both the levels of u_1 itself, and the levels of other components by looking at the effect on a component u_2. As for our simulations of full RD systems we performed two forms of inhibition, namely inhibiting the response of a component to the levels of u_1 (analogous to inhibiting a "u_1 receptor") and inhibiting the production of u_1.

2.1.1: Inhibition of response to u_1

We first consider the effect of perturbing the response to u_1 by multiplying the weight of all interactions from component u_1 (to itself and all other components) by a factor of $1 - \alpha$ (i.e. with no inhibition when $\alpha = 0$ and complete inhibition when $\alpha = 1$). At equilibrium, this gave a system of the form

$$\frac{du_1}{dt} = 0 = (1 - \alpha)a_{11}u_1 + \sum_{j=2}^{N} a_{1j}u_j + b_1 - c_1u_1$$

and

$$\frac{du_i}{dt} = 0 = (1 - \alpha)a_{i1}u_i + \sum_{j=2}^{N} a_{ij}u_j + b_i - c_iu_i, \qquad i = 2, \dots, N.$$

It should be noted that for the response of u_1 to its own inhibition, only the weight of a_{11} is reduced, as c_1 represents a linear degradation term and would therefore be unaffected directly by an inhibitor blocking a receptor.

Rearranging these equations gave equilibrium levels of u_i upon inhibition of strength α, where

$$u_1 = -\frac{\sum_{j=1}^{N} \mathrm{C}[\boldsymbol{A}]_{j1} b_j}{\det[\boldsymbol{A}] - \alpha \det[\boldsymbol{C}]} \quad (2.1)$$

and

$$u_i = -\frac{\sum_{j=1}^{N} \mathrm{C}[\boldsymbol{A}]_{ji} b_j - \alpha \sum_{j=1}^{N} \mathrm{C}[\boldsymbol{C}]_{ji} b_j}{\det[\boldsymbol{A}] - \alpha \det[\boldsymbol{C}]} \quad (2.2)$$

for i=2,…,N. Matrix $\mathbf{C}$, which does not include the degradation term c_1, is given by

$$\boldsymbol{C} = \begin{pmatrix} a_{11} & a_{12} & \cdots & a_{1N} \\ a_{21} & a_{22} - c_2 & \cdots & a_{2N} \\ \vdots & \vdots & \ddots & \vdots \\ a_{N1} & a_{N2} & \cdots & a_{NN} - c_N \end{pmatrix},$$

and $\mathrm{C}[\boldsymbol{C}]_{ji}$ is the cofactor of the element of the j^{th} row and i^{th} column of $\boldsymbol{C}$.

Response of u_1:

The response of u_1 to its own inhibition is governed by Equation (2.1), which is a function of α with horizontal and vertical asymptotes at

$u_1 = 0$

and

$$\alpha = \frac{\det[\boldsymbol{A}]}{\det[\boldsymbol{C}]},$$

respectively. The intercept of the u_1-axis lies at

$$u_1 = -\frac{\sum_{j=1}^{N} \mathrm{C}[\boldsymbol{C}]_{j1} b_j}{\det[\boldsymbol{A}]},$$

which is the unperturbed level of u_1 (i.e. when $\alpha = 0$). As the unperturbed level of u_1 has a positive value, the function in Equation (2.1) can take two forms, depending on whether the vertical asymptote corresponds to a positive or negative value of α (see Figure SN1 a).

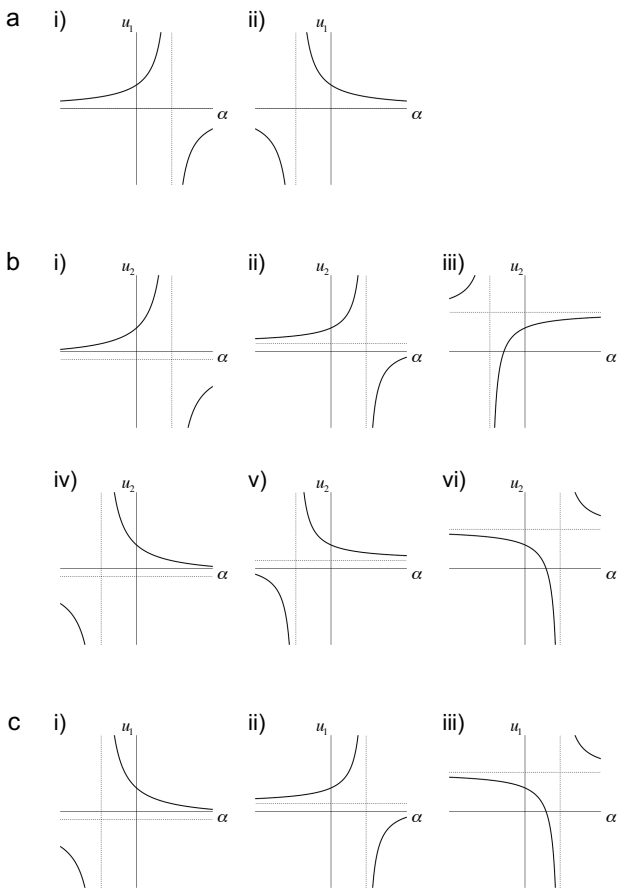

Figure SN1
a) Graphs showing the two possible responses of u_1 to the inhibition of u_1 by strength α. The vertical asymptote (dashed line) can lie at a positive (i) or negative (ii) value of α. The horizontal asymptote lies along the α-axis.
b) Graphs showing the six possible responses of u_2 to the inhibition of u_1 by strength α. The vertical asymptote (vertical dashed line) can lie at a positive (i, ii and vi) or negative (iii, iv and v) value of α. The horizontal asymptote (horizontal dashed line) can lie at a positive (ii, iii, v and vi) or negative (i and iv) value of u_2. The intercept of the α-axis can lie at a positive (ii, iv and vi) or negative (i, iii and v) value of α.
c) Graphs showing the three possible responses of $u_1$to the inhibition of u_1 by strength α. The vertical asymptote (vertical dashed line) can lie at a positive (ii and iii) or negative (i) value of α. The horizontal asymptote (horizontal dashed line) can lie at a positive (ii and iii) or negative (i) value of u_1. The intercept of the α-axis can lies at α=1.

Therefore, u_1 will increase with its own inhibition if

$$\frac{\det[\boldsymbol{A}]}{\det[\boldsymbol{C}]} > 0 \quad (2.3)$$

and will decrease if

$$\frac{\det[\boldsymbol{A}]}{\det[\boldsymbol{C}]} < 0. \quad (2.4)$$

Response of u_2:

The response of u_2 to inhibition of u_1 is governed by Equation (2.2), which is also a function of α with horizontal and vertical asymptotes, which lie at

$$u_2 = -\frac{\sum_{j=1}^{N} \mathrm{C}[\boldsymbol{C}]_{j2} b_j}{\det[\boldsymbol{C}]}$$

and

$$\alpha = \frac{\det[\boldsymbol{A}]}{\det[\boldsymbol{C}]},$$

respectively. The intercept of the u_2-axis lies at

$$u_2 = -\frac{\sum_{j=1}^{N} \mathrm{C}[\boldsymbol{A}]_{j2} b_j}{\det[\boldsymbol{A}]},$$

which is the unperturbed state (when $\alpha = 0$) and has a positive value, while the intercept of the α-axis is at

$$\alpha = \frac{\sum_{j=1}^{N} \mathrm{C}[\boldsymbol{A}]_{ji} b_j}{\sum_{j=1}^{N} \mathrm{C}[\boldsymbol{C}]_{ji} b_j}.$$

Depending on the relative values of the asymptotes and intercepts, this function can take six forms (Figure SN1 b), for three of which (Figure SN1 b i–iii), u_2 increases with inhibition of u_1. For the remaining three (Figure SN1 b iv–vi), u_2 decreases with the inhibition of u_1. From the positions of the horizontal asymptote relative to the unperturbed state at $\alpha = 0$, for conditions i, ii, iv and v

$$-\frac{\sum_{j=1}^{N} \mathrm{C}[\boldsymbol{A}]_{j2} b_j}{\det[\boldsymbol{A}]} > -\frac{\sum_{j=1}^{N} \mathrm{C}[\boldsymbol{C}]_{j2} b_j}{\det[\boldsymbol{C}]},$$

while for conditions iii and vi

$$-\frac{\sum_{j=1}^{N} \mathrm{C}[\boldsymbol{A}]_{j2} b_j}{\det[\boldsymbol{A}]} < -\frac{\sum_{j=1}^{N} \mathrm{C}[\boldsymbol{C}]_{j2} b_j}{\det[\boldsymbol{C}]}.$$

However, from the position of the vertical asymptote, for i, ii and vi

$$\frac{\det[\boldsymbol{A}]}{\det[\boldsymbol{C}]} > 0,$$

while for iii, iv and v

$$\frac{\det[\boldsymbol{A}]}{\det[\boldsymbol{C}]} < 0.$$

Therefore, in conditions i, ii and iii, where u_2 increases on the inhibition of u_1,

$$\det[\boldsymbol{C}] \sum_{j=1}^{N} \mathrm{C}[\boldsymbol{A}]_{j2} b_j < \det[\boldsymbol{A}] \sum_{j=1}^{N} \mathrm{C}[\boldsymbol{C}]_{j2} b_j, \quad (2.5)$$

while in conditions iv, v and vi, where u_2 decreases on the inhibition of u_1,

$$\det[\boldsymbol{C}] \sum_{j=1}^{N} \mathrm{C}[\boldsymbol{A}]_{j2} b_j > \det[\boldsymbol{A}] \sum_{j=1}^{N} \mathrm{C}[\boldsymbol{C}]_{j2} b_j. \quad (2.6)$$

2.1.2: Inhibition of production of u_1

We next considered the effect of inhibiting the production of u_1 by reducing the weights of all the coefficients affecting the production of u_1 (including the constant term, but excluding the degradation coefficient) by a factor of 1-α. At equilibrium, this gives a system of the form

$$\frac{du_1}{dt} = 0 = (1-\alpha)\left(\sum_{j=1}^{N} a_{1j} u_j + b_1\right) - c_1 u_1$$

and

$$\frac{du_i}{dt} = 0 = \sum_{j=1}^{N} a_{ij}u_j + b_i - c_i u_i$$

for i=2,…,N. Rearranging these equations gives the equilibrium levels of u_i upon inhibition of strength α, where

$$u_1 = -\frac{\sum_{j=1}^{N} \mathrm{C}[\boldsymbol{A}]_{j1} b_j (1-\alpha)}{\det[\boldsymbol{A}] - \alpha \det[\boldsymbol{C}]} \quad (2.9)$$

and

$$u_i = -\frac{\sum_{j=1}^{N} \mathrm{C}[\boldsymbol{A}]_{ji} b_j - \alpha \sum_{j=1}^{N} \mathrm{C}[\boldsymbol{C}]_{ji} b_j}{\det[\boldsymbol{A}] - \alpha \det[\boldsymbol{C}]}$$

for i=2,…,N. As the equation giving the equilibrium value of u_i where $i \neq 1$ is the same as that for the inhibition of the response (Equation (2.2)), the shape of the response of u_2 to an inhibition of strength α is the same for inhibiting either the production of, or the response to, u_1.

Behaviour of u_1:

The behaviour of the equilibrium value of u_1 is again governed by a function of α (Equation (2.9)) with horizontal and vertical asymptotes, which now lie at

$$u_1 = -\frac{\sum_{j=1}^{N} \mathrm{C}[\boldsymbol{A}]_{j1} b_j}{\det[\boldsymbol{C}]}$$

and

$$\alpha = \frac{\det[\boldsymbol{A}]}{\det[\boldsymbol{C}]},$$

respectively. The intercept of the u_1-axis lies at

$$u_1 = -\frac{\sum_{j=1}^{N} \mathrm{C}[\boldsymbol{A}]_{j1} b_j}{\det[\boldsymbol{A}]},$$

which is the unperturbed state and has a positive value, while the intercept of the α-axis is at $\alpha = 1$.

Depending on the relative positions of the asymptotes and intercepts, this function can take three forms (Figure SN1 c), for two of which (Figure SN1 c i, iii), the equilibrium value of u_1 decreases with its inhibition, while for the remaining one (Figure SN1 c ii), the equilibrium value of u_1 increases with its inhibition. Therefore, the equilibrium value of u_1 will increase on its inhibition if

$$\frac{\det[\boldsymbol{A}]}{\det[\boldsymbol{C}]} < 0 \quad (2.10)$$

or

$$\frac{\det[\boldsymbol{A}]}{\det[\boldsymbol{C}]} > 1. \quad (2.11)$$

While the equilibrium value of u_1 will decrease on its inhibition if

$$0 < \frac{\det[\boldsymbol{A}]}{\det[\boldsymbol{C}]} < 1. \quad (2.12)$$

2.2: Comparison with a numerically modelled RD system

Using this framework, we could compare the responses to inhibition for the full 2- and three-component RD systems with the behaviour of the reaction terms. We took the parameterisations of the reaction terms used in the full RD simulations (Figure 3 and Supplementary Figure S11) and inferred the direction of response by calculating the relative position of the asymptotes and intercepts. Comparison of the direction of the response to an inhibition for the reaction terms alone and for the full RD system (Figure SN2) showed that the pattern of the responses is very similar. This suggests that the response to an inhibition is predominantly dictated by the response of the reaction terms.

What about the small proportion of parameterisations for which the response of the equilibrium values differs between the full RD system and the analysis of the reaction terms alone? Interestingly, repeating the simulations, but reducing the strength of the inhibition by a factor of 0.25 or 0.25^2, successively increased the discrepancy (Figure SN2). As decreasing the strength of an inhibition decreases the magnitude of the response for the reaction terms, this suggests that the response of the reaction terms will dictate the response of the full RD system provided that the responses are sufficiently large. As the only difference between the reaction term systems and the full RD systems is diffusion, this suggests that if the response to an inhibition of the reaction terms is not sufficiently large, there can be a significant effect of diffusion, which in some cases can change the direction of response generated by the reaction terms alone.

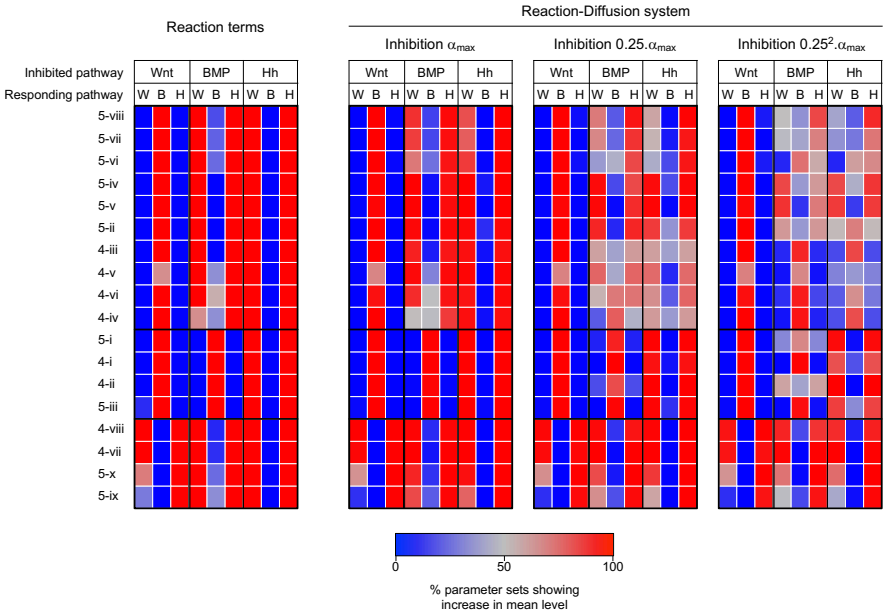

Figure SN2
Full maps showing the percentage of parameter sets where the level of each component increases in response to the inhibition of each component in the network in reaction term analysis and in RD simulations. The left hand heat map shows the response for reaction term analysis for the parameter sets used in three-component RD analysis, evaluated using criteria from Section 2. The second heat map, showing the Reaction-Diffusion system with inhibition strength α_{max}, is a reproduction of the heat map from Figure 3, and the heat maps with inhibition strength $0.25.\alpha_{max}$ and $0.25^2.\alpha_{max}$ are from reruns of the three-component RD simulations, replacing the inhibition parameter value α with values of $0.25.\alpha$ and $0.25^2.\alpha$ respectively. Pathway topology names are as in Figure 3.

This is likely to be generally true for RD systems based on the following argument. Large perturbations in reaction terms will produce large shifts in the mean value of the periodic pattern while changes in the diffusion terms will flatten or sharpen the peaks and troughs. For example, an increase in the reaction term will increase the value of u_i in both peaks and troughs.

For equilibrium to be restored, the diffusion term $D_i \frac{\partial^2 u_i}{\partial x^2}$ has to decrease. Since at the peaks, $D_i \frac{\partial^2 u_i}{\partial x^2}$ is negative, this means it has to become more negative, i.e. the peaks must become sharper. Conversely, the troughs must become flatter (the positive second derivative becomes less positive). These changes in the curvature of the peaks and troughs do not necessarily have a net effect on the average levels that are the same or opposite to the reaction term change. Our simulations, however, say that their effects do not increase at the same rate as those of the reaction terms. The simulations suggest that their role is more pronounced for small reaction term changes although we have not been able to demonstrate this analytically.

3: A graphical interpretation of the responses to perturbation

We wanted to understand how the position of a component in a network affects the response of the system to its inhibition. In particular, we wanted to understand how the response depends on the type of feedback loop the component is found in. In a recent study Marcon et al. (2016) used such a graphical approach to understand the conditions for DDI, in terms of stabilizing and destabilizing contributions of different feedback loops. This was based on an interpretation of the determinant as a combination of the cycles defined by the reaction matrix. As the conditions determining the response to perturbation (see Section 2) are in part dependent on the determinants of matrices $\boldsymbol{A}$ and $\boldsymbol{C}$, we took a similar approach.

In brief, a matrix $\boldsymbol{M}$ (such as the reaction matrices $\boldsymbol{A}$ and $\boldsymbol{C}$, or in the approach of Marcon et al. the Jacobian matrix $\boldsymbol{J}$) has associated graph Gr[$\boldsymbol{M}$] which is a labelled, weighted, directed graph of N nodes with edges from node j to node i of weight a_{ij}, where $a_{ij} \neq 0$ are the elements of the matrix $\boldsymbol{M}$. This is the graphical representation of the reaction network that we have been using throughout to depict the signs of the interactions as a network topology. Such a graph contains cycles, where a path can be traced from any node, through a series of other nodes, back to itself (or directly onto itself without passing through any other nodes). A cycle represents a positive feedback loop if the product of the weights of the edges is positive, and a negative feedback loop if the product is negative.

For any graph Gr[$\boldsymbol{M}$], a subgraph can be defined containing all the nodes but only a subset of the edges of Gr[$\boldsymbol{M}$], such that each node receives an input from only one other node and also outputs to only one other node (i.e. each node has both an in-degree and out-degree of 1). Such a subgraph is called a linear spanning subgraph (L-subgraph, l), and is made up of a set of 1 to N cycles through all nodes. The weight of an L-subgraph $w(l)$ is given by the product of the weights of these cycles, with the weight of each cycle itself being the product of its constituent edges. The determinant of the $N \times N$ matrix $\boldsymbol{M}$ is given by the sum of the weights of all the L-subgraphs l of the graph Gr[$\boldsymbol{M}$], with signs as below

$$\det[\boldsymbol{M}] = (-1)^N \sum_{l \subseteq Gr[\boldsymbol{M}]} (-1)^{\sigma(l)} w(l), \quad (3.1)$$

where σ(l) is the number of cycles in the L-spanning subgraph l. Equation (3.1) is known as the Coates formula; for more details on the derivation, see Marcon et al. (2016) and references therein.

3.1: Response of u_1

As demonstrated in Section 2, the response of u_1 to its own inhibition depends on the sign and magnitude of the ratio of det[$\boldsymbol{C}$] to det[$\boldsymbol{A}$]. The sign is determined by the criteria for a DDI (see Section 1). To understand the response of u_1 to its own inhibition in graphical terms, we therefore considered these determinants in terms of the feedback loops (or cycles) through u_1 in matrix $\boldsymbol{C}$. From Equation (3.1), each summand in det [$\boldsymbol{C}$] can be written in the form $(-1)^N(-1)^{\sigma(l)}w(l)$, where l is a linear spanning subgraph of Gr[$\boldsymbol{C}$]. As all nodes in an l-graph have an in-degree and an out-degree of 1, for each summand in Equation (3.1) there is a single cycle containing node u_1, which comprises a set of n nodes, where $1 \leq n \leq N$, with κ_n a sequence of integers {i_1,i_2,…,i_n} which defines the sequence of nodes u_i through which the cycles passes, with each such sequence starting at i_1=1. If n=1, the cycle forms an interaction from u_1 directly onto itself, while if n=N, the cycle passes through all nodes. S_{κ_n} is the set of all possible κ_n, and $w(\kappa_n)$ is the weight of the cycle defined by κ_n (positive for a positive feedback loop, negative for a negative feedback loop). For each such cycle, where n<N, the nodes excluded from the cycle form an L-graph l_n consisting of 1 to N-n cycles between the remaining nodes, where $\sigma(l_n)$ is the number of remaining cycles (with $\sigma(l_n) = \sigma(l) - 1$ as one cycle has been removed). $w(l_n)$ is the product of the weights of the remaining cycles such that $w(l) = w(\kappa_n)w(l_n)$, and S_{l_n} is the set of all possible L-graphs l_n for a given κ_n.

Therefore, for any term in the determinant, the loop through u_1 can be factored out to give

$$(-1)^N(-1)^{\sigma(l)}w(l) = -(-1)^n w(\kappa_n)(-1)^{N-n}(-1)^{\sigma(l_n)}w(l_n).$$

Gathering together determinant terms containing the same cycle through u_1, the determinant can be rewritten

$$\det[\boldsymbol{C}] = -\sum_{\kappa_n \subseteq S_{\kappa_n}} (-1)^n w(\kappa_n)(-1)^{N-n} \sum_{l_n \subseteq S_{l_n}} (-1)^{\sigma(l_n)} w(l_n)$$

$$= -\sum_{\kappa_n \subseteq S_{\kappa_n}} (-1)^n w(\kappa_n) \det[\boldsymbol{C}(\tilde{\kappa}_n)], \quad (3.2)$$

where $\boldsymbol{C}(\tilde{\kappa}_n)$ is the submatrix of $\boldsymbol{C}$ excluding the columns and rows defined in κ_n (for n=N, $\det[\boldsymbol{C}(\tilde{\kappa}_n)] = 1$, as it is the determinant of a 0×0 matrix).

3.1.1: Inhibiting the response to u_1

As demonstrated in Section 2, the behaviour of u_1 on inhibiting the response to u_1 is dependent on whether the ratio $\frac{\det[\boldsymbol{A}]}{\det[\boldsymbol{C}]}$ is positive or negative (see Equations (2.3) and (2.4)). Therefore, u_1 will increase in response to its own inhibition if

$$\frac{\sum_{\kappa_n \subseteq S_{\kappa_n}} (-1)^n w(\kappa_n) \det[\boldsymbol{C}(\tilde{\kappa}_n)]}{\det[\boldsymbol{A}]} < 0 \quad (3.3)$$

and will decrease if

$$\frac{\sum_{\kappa_n \subseteq S_{\kappa_n}} (-1)^n w(\kappa_n) \det[\boldsymbol{C}(\tilde{\kappa}_n)]}{\det[\boldsymbol{A}]} > 0, \quad (3.4)$$

where each summand contains a different cycle through u_1, each multiplied by the determinant of the submatrix made of components excluded from the cycle. The response of u_1 to the inhibition of its response therefore depends on the natures of the feedback loops through u_1, and the stability of the components excluded from the loops.

3.1.2: Inhibiting the production of u_1

For inhibiting the production of u_1, we demonstrated in Section 2 that the response of u_1 again depends on $\det[\boldsymbol{A}]$ and $\det[\boldsymbol{C}]$ (see inequalities 2.10 – 2.12). First considering when N is even,

from Section 1 it follows that $\det[\boldsymbol{A}] > 0$. To satisfy the condition (2.10), $\det[\boldsymbol{C}] < 0$, and as a consequence, $\det[\boldsymbol{A}] > \det[\boldsymbol{C}]$. Otherwise, $\det[\boldsymbol{C}] > 0$, and in this case, to also satisfy condition (2.11), it follows that again $\det[\boldsymbol{A}] > \det[\boldsymbol{C}]$. However, when condition (2.12) holds, it follows that $\det[\boldsymbol{A}] < \det[\boldsymbol{C}]$. Therefore, when $\det[\boldsymbol{A}] < \det[\boldsymbol{C}]$, u_1 increases when its production is inhibited, while when $\det[\boldsymbol{A}] > \det[\boldsymbol{C}]$, u_1 decreases when its production is inhibited.

As matrices $\boldsymbol{A}$ and $\boldsymbol{C}$ only differ by the presence or absence of the $-c_1$ in the first matrix term, then

$$\det[\boldsymbol{A}] = \det[\boldsymbol{C}] - c_1 \det[\boldsymbol{C}(\tilde{\kappa}_1)],$$

where $\boldsymbol{C}(\tilde{\kappa}_1)$ is the submatrix of $\boldsymbol{C}$, excluding the first row and column. It therefore follows that u_1 will increase following its own inhibition if

$$c_1 \det[\boldsymbol{C}(\tilde{\kappa}_1)] > 0,$$

and u_1 will decrease following its own inhibition if

$$c_1 \det[\boldsymbol{C}(\tilde{\kappa}_1)] < 0.$$

Given that $c_1 > 0$, it follows that u_1 will increase when its production is inhibited if

$$\frac{\det[\boldsymbol{C}(\tilde{\kappa}_1)]}{\det[\boldsymbol{A}]} > 0, \quad (3.5)$$

and will decrease when

$$\frac{\det[\boldsymbol{C}(\tilde{\kappa}_1)]}{\det[\boldsymbol{A}]} < 0. \quad (3.6)$$

By the same reasoning, these conditions also hold if N is odd. The response of u_1 to the inhibition of its production therefore depends on the stability of the submatrix made from the remaining components.

3.2: Response of u_2:

As demonstrated in Section 2 (Equations (2.5) and (2.6)), the response of component u_2 in an N-component system to the inhibition of u_1 is in part determined by the relative signs and sizes of the determinants det[$\boldsymbol{A}$] and det[$\boldsymbol{C}$]. The response to inhibition also depends on the terms $\sum_{j=1}^{N} \mathrm{C}[\boldsymbol{A}]_{j2} b_j$ and $\sum_{j=1}^{N} \mathrm{C}[\boldsymbol{C}]_{j2} b_j$, which are of the same form as a determinant, but with the second column of matrix $\boldsymbol{A}$ and $\boldsymbol{C}$ respectively replaced by the vector of background production terms (b_1,b_2,…,b_N). Therefore, each term in these sums can similarly be interpreted graphically, as a path from an external node u_b to component u_2, with all components not involved in the path making up a set of cycles with each node having an in-degree and an out-degree of 1. Therefore, for each summand, every node has a single input and a single output, except u_b, which only has a single output and no input, and u_2, which only has a single input and no output.

Conditions (2.5) and (2.6) can be rearranged to give

$$c_1 \sum_{j=2}^{N} \mathrm{C}[\boldsymbol{C}(\tilde{\kappa}_1)]_{(j-1)1} a_{j1} \sum_{j=1}^{N} \mathrm{C}[\boldsymbol{A}]_{j1} b_j > 0 \qquad (3.7)$$

and

$$c_1 \sum_{j=2}^{N} \mathrm{C}[\boldsymbol{C}(\tilde{\kappa}_1)]_{(j-1)1} a_{j1} \sum_{j=1}^{N} \mathrm{C}[\boldsymbol{A}]_{j1} b_j < 0, \qquad (3.8)$$

respectively, where $\mathrm{C}[\boldsymbol{C}(\tilde{\kappa}_1)]_{(j-1)1}$ is the cofactor of the term a_{j2} from matrix $\boldsymbol{C}$ in the submatrix $\boldsymbol{C}(\tilde{\kappa}_1)$ (as this submatrix excludes the first row and column of $\boldsymbol{C}$, this will be the cofactor of the first column and the (j-1)th row).

The only term in conditions (3.7) and (3.8) whose sign is not constrained is $\sum_{j=2}^{N} \mathrm{C}[\boldsymbol{C}(\tilde{\kappa}_1)]_{(j-1)1} a_{j1}$. From Equations (2.1) and (2.9), which describe the levels of u_1 under inhibition, for the unperturbed state of u_1 to be positive, the term $\sum_{j=1}^{N} \mathrm{C}[\boldsymbol{A}]_{j1} b_j$ must have the same sign as the determinant det [$\boldsymbol{A}$] (positive if there are an even number of components and negative if there are an odd number). Also, $-c_1 < 0$ as it represents a degradation term. The form of the sum $\sum_{j=2}^{N} \mathrm{C}[\boldsymbol{C}(\tilde{\kappa}_1)]_{(j-1)1} a_{j1}$ is the same as that of $\sum_{j=1}^{N} \mathrm{C}[\boldsymbol{A}]_{j1} b_j$, and so it can be

interpreted as a sum where each term represents a path from component u_1 to component u_2. Specifically,

$$\sum_{j=2}^{N} \mathrm{C}[\boldsymbol{A}(\tilde{\kappa}_1)]_{(j-1)1} a_{j1} = -\sum_{p_n \subseteq S_{p_n}} (-1)^n w(p_n) \det[\boldsymbol{A}(\tilde{\kappa}_n)], \quad (3.9)$$

where p_n is a sequence of integers $\{i_1,i_2,\ldots,i_n\}$, where $2 \leq n \leq N$, starting with i_1=1 and ending with i_n=2, which defines the series of nodes u_i through which the path from u_1 to u_2 passes, S_{p_n} is the set of all possible such paths, and $w(p_n)$ the weight of the path p_n. The response of u_2 to the inhibition of u_1 therefore depends on the weight of the paths between the two nodes, and the stability of the components excluded from the paths.

4: Constraints on minimal topologies

Having established graphical conditions for the response of a system to inhibition of each component, we wanted to establish how the response of the system is related to network topology. As with our numerical investigation of three-component systems, we set out to understand the behavior of the subset of networks with the minimal requirements for patterning. We first establish the minimal requirements for a strongly-connected RD system, before considering how these networks respond to perturbation. We note that this subject has recently been dealt with extensively by Marcon et al and Diego et al, although as we assume all components degrade by default, we use a slightly different definition of minimal.

4.1: Identifying minimal topologies

4.1.1: Minimal conditions for a DDI

In order to establish the minimal requirements for DDI we asked what are the fewest interactions (excluding degradation terms) and feedback loops needed to satisfy the criteria for DDI. It should be noted that as we have been using a system of linear equations in our reaction-diffusion system, the reaction matrix $\boldsymbol{A}$ is the same as the Jacobian matrix $\boldsymbol{J}$, and the number of interactions is given by the number of non-zero terms a_{ij}. As described in Section 1, conditions for DDI that will always give rise to monotonically growing patterns require that $a_N(q^2) < 0$. Considering the terms that make up $a_N(q^2)$ (Equation (1.1)), the first term is made up solely of reaction terms and requires that $(-1)^N \det[\boldsymbol{J}] > 0$ in order to satisfy the criterion of stability in the absence of diffusion ($a_N(0) > 0$). The third term is made up solely of diffusion coefficients and the wavelength coefficient q^2, both of which are positive, meaning that $q^{2N} det[\boldsymbol{D}] > 0$. For the remaining terms, which contain both reaction and diffusion coefficients, as above for the diffusion and wavelength coefficients $q^{2(N-m)} \det[\boldsymbol{D}(\bar{\gamma}_m)] > 0$. Therefore, the conditions for DDI depend on the reaction terms and the signs of the various terms $(-1)^m \det[\boldsymbol{J}(\gamma_m)]$.

We first considered a system consisting of N components, without any interactions between them. These components will be only undergoing degradation (i.e. the only non-zero terms in $\boldsymbol{J}$ are on the diagonal, and are negative or in terms of reaction matrix $\boldsymbol{A}$, for all coefficients a_{ij}=0). From Equation (3.1), the only non-zero summands of any of the submatrix determinants

$\det[\boldsymbol{J}(\gamma_m)]$ in Equation (1.1) will be those consisting only of self-interactions (i.e. the degradation terms). It therefore follows that

$$(-1)^m \det[\boldsymbol{J}(\gamma_m)] = (-1)^m \prod_{i=1}^{m} J_{(\gamma_m)_i(\gamma_m)_i}, \quad (4.1)$$

which will always have a positive sign. Therefore, unsurprisingly, the condition for instability when there is diffusion cannot be satisfied in this simple system, since $a_N(q^2) < 0$.

In order to satisfy the conditions for DDI there must be at least one term in $a_N(q^2)$ with a negative sign. From Equation (4.1) this can be achieved by simply adding a single auto-activation term for a component. For example, if u_1 directly activates itself, providing that this auto-activation is strong enough to outweigh the degradation term for u_1 (in terms of matrix $\boldsymbol{A}$, $a_{11} - c_1 > 0$), a single term on the diagonal of the Jacobian matrix J_{11} will go from being negative to positive, resulting in the sign of any term $\det[\boldsymbol{J}(\gamma_m)]$ for which γ_m contains u_1 also changing sign. Alternatively, this can also be achieved by the addition of a single positive feedback loop through the set of r nodes defined by the sequence γ_r of weight $w(\gamma_r)$. For any $\det[\boldsymbol{J}(\gamma_m)]$ where γ_r is a subset of γ_m

$$\det[\boldsymbol{J}(\gamma_m)] = \left(\prod_{i=1}^{r} J_{(\gamma_r)_i(\gamma_r)_i} - (-1)^r w(\gamma_r) \right) \prod_{j=1}^{m-r} J_{(\tilde{\gamma}_r)_j(\tilde{\gamma}_r)_j},$$

where $\tilde{\gamma}_r$ is a complementary sequence of integers to γ_r such that $\gamma_r \cap \tilde{\gamma}_r = 0$ and $\gamma_r \cup \tilde{\gamma}_r = \gamma_m$. Again, provided that the weight of the positive feedback loop is greater than for the degradation terms, $\det[\boldsymbol{J}(\gamma_m)]$ will change sign.

However, as the sign of any submatrix containing the positive feedback loop will change sign, it follows that with the addition of a single destabilising positive feedback loop, $(-1)^N \det[\boldsymbol{J}] < 0$. This will no longer satisfy the condition for stability in the absence of diffusion $a_N(0) > 0$. An additional positive summand in $a_N(0)$ is therefore needed to stabilize the system. By the above reasoning, this can most simply be achieved by the addition of a single negative feedback between a set of components γ_s, where $\gamma_s \neq \gamma_r$. If this negative feedback loop takes the form of a path from a node γ_r, through the remaining nodes in the system and back into any node in γ_r, a single additional term will be added to any $\det[\boldsymbol{J}(\gamma_m)]$ where γ_s is a subset of γ_m (including

those for which γ_r is also a different subset). If the weight of this loop is sufficiently large, then it can overcome the effect of the positive feedback loop, and satisfy $a_N(0) > 0$.

Moreover, as there will still exist γ_m for which γ_r is a subset, but not γ_s, there will be terms $q^{2(k-m)}(-1)^m \det[\boldsymbol{J}(\gamma_m)] \det[\boldsymbol{D}(\tilde{\gamma}_m)]$ which will remain negative, even after the addition of a negative feedback loop to the system. Therefore, with the appropriate weighting of diffusion coefficients, there will exist conditions where $a_k(q^2) < 0$ when k=N, but not for other k, while maintaining $a_N(0) > 0$. As such $\tilde{\gamma}_m$ will by definition exclude components of the positive feedback loop through the nodes in γ_r, to achieve such a weighing, diffusion coefficients among components in the negative will be larger than those in the positive feedback loop. This gives an intuitive understanding for then general idea of local auto-activation and long-range inhibition in RD systems. In summary, a system containing single positive feedback loop coupled to a negative feedback loop is, therefore, sufficient to satisfy the conditions for a DDI for any size system, given appropriate strengths of interactions and diffusion coefficients.

Considering the minimal requirements for DDI in terms of the number of interactions between components in the interaction matrix $\boldsymbol{A}$ (including auto-activation terms a_{ii}, but not degradation terms c_i), in any such system a positive feedback loop through r components will add r interactions to the system, while the negative feedback loop though the remaining N-r components will add a further N-r+1 terms, resulting in a total of N+1 interactions. For any strongly-connected network, it is clear than fewer than N+1 interactions will not allow sufficient feedback loops to be made to satisfy the criteria for DDI, while other networks made of N+1 interactions (e.g. two positive or two negative feedback loops) cannot satisfy the conditions for DDI. While there are other ways of satisfying these conditions, they will require additional feedback loops, and therefore additional interaction. Therefore, in a system of N components, the combination of a single positive feedback loop through one to N-1 components, and a negative feedback loop through the remaining components is the minimal requirement for a DDI.

4.1.2: The phase of minimal DDI systems

Having established the architecture of minimal topologies, we next sought to establish the relative phase of the components for each of these topologies. This is dictated by the signs of

the components of the eigenvector corresponding to the largest positive eigenvalue of the Jacobian matrix: components with the same sign will be in the same phase. From the derivation of conditions for DDI in Section 1, we have the relationship

$$\begin{pmatrix} J_{11} - D_1 q^2 - \lambda & J_{12} & \cdots & J_{1N} \\ J_{21} & J_{22} - D_2 q^2 - \lambda & \cdots & J_{2N} \\ \vdots & \vdots & \ddots & \vdots \\ J_{N1} & J_{N2} & \cdots & J_{NN} - D_N q - \lambda \end{pmatrix} \begin{pmatrix} u_1 \\ u_2 \\ \vdots \\ u_N \end{pmatrix} = 0.$$

For all minimal architectures, there is only one component that receives more than one input (excluding negative self-interactions). For all remaining components, the rows in the matrix will consist of only two non-zero terms: the degradation term on the diagonal, J_{ii} which is therefore negative, and an additional input term from another component J_{ij}, whose sign depends on the nature of the input. Therefore, each of these rows will take the form

$$(J_{ii} - D_i q^2 - \lambda)u_i + J_{ij}u_j = 0.$$

By definition, for a DDI λ>0, meaning that $J_{ii} - D_i q^2 - \lambda < 0$. Consequently, u_i and u_j will have the same sign, and therefore be in-phase with each other if J_{ij} is positive, while they will have opposing signs and be out-of-phase for negative J_{ij}. Therefore, the relative phase of successive components in the positive and negative feedback loops can be inferred from the signs of interaction between them, with the exception of the interaction from a component in the negative feedback loop feeding into the positive feedback loop. Moreover, two components will be in-phase if the weight of the path between them is positive, and out-of-phase if negative, unless the path passes from the negative feedback loop into the positive feedback loop, in which case the relationship will be reversed. This is in keeping with recent finding on the relationship between topology and phase by Diego et al.

4.2: Responses to perturbation of minimal topologies

Having established minimal conditions for DDI, we next asked how these minimal systems respond to the inhibition of the different components. In particular, as these systems consist only of a single positive and a single negative feedback loop, we considered how the response to inhibition depends on the placement of a component relative to these two loops.

4.2.1: Inhibition of response

For the inhibition of response to u_1, in Section 3.1.1, conditions (3.3) and (3.4), it was shown that the response is dependent on the sign of

$$\frac{\sum_{\kappa_n \subseteq S_{\kappa_n}} (-1)^n w(\kappa_n) \det[\boldsymbol{C}(\tilde{\kappa}_n)]}{\det[\boldsymbol{A}]}, \quad (4.2)$$

where each summand corresponds to a different feedback loop through u_1. For minimal topologies, the sign of each summand depends on two features: whether the feedback loop supported by u_1 is a positive or negative feedback loop (given by $w(\kappa_n)$), and whether the nodes excluded from this loop support a positive feedback loop (given by $\det[\boldsymbol{C}(\tilde{\kappa}_n)]$). For each summand, $w(\kappa_n)$ will be negative if it represents a negative feedback loop and positive for a positive feedback loop. However, the relationship between the sign of $\det[\boldsymbol{C}(\tilde{\kappa}_n)]$, and the feedback loops contained depends on the number of nodes in the system described by submatrix $\boldsymbol{C}(\tilde{\kappa}_n)$ (see Section 1). Considering all possible combinations of odd and even numbers of components in matrix $\boldsymbol{A}$ and submatrix $\boldsymbol{C}(\tilde{\kappa}_n)$, it can be seen that $(-1)^n \det[\boldsymbol{C}(\tilde{\kappa}_n)] / \det[\boldsymbol{A}]$ will always be negative if submatrix $\boldsymbol{C}(\tilde{\kappa}_n)$ contains a single positive feedback loop, and will be positive if it only contains negative feedback loops.

As minimal systems only contain a single positive feedback loop and a single negative feedback loop, submatrix $\boldsymbol{C}(\tilde{\kappa}_n)$ will always contain only negative feedback loops as the two loops must share at least one component. Therefore, each summand in Equation (4.2) will be positive if it represents a positive feedback loop and negative if it represents a negative feedback loop. For certain placements in a minimal network, u_1 will only fall in one feedback loop, and there will be a single non-zero summand in Equation (4.2). Therefore, if u_1 is only found in the positive feedback loop it will decrease on its inhibition, and if it is found only in the negative feedback loop it will increase on its inhibition. However, for some placements in a minimal network u_1 will be in both positive and negative feedback loops. In these instances, there will be two summands in Equation (4.2), one positive and the other negative. The response of the system will depend on the relative magnitude of each term, with both an increase and a decrease in u_1 possible. These constraints are summarised in Figure 4b.

4.2.2: Inhibition of production

As shown in Section 3.1.2, conditions (3.5) and (3.6), the response of u_1 to the inhibition of its own production is determined by the sign of $\det[\boldsymbol{C}(\tilde{\kappa}_1)]$ relative to $\det[\boldsymbol{A}]$. This in turn, depends on whether the system described by the submatrix excluding u_1 contains the positive feedback loop of the minimal network or not. If u_1 is excluded from the positive feedback loop, the submatrix determinant $\det[\boldsymbol{C}(\tilde{\kappa}_1)]$ will therefore contain the single positive feedback loop in the system. As matrix $\boldsymbol{C}(\tilde{\kappa}_1)$ by definition has one fewer component than matrix $\boldsymbol{A}$, as detailed in equation 3.1, $\det[\boldsymbol{A}]$ and $\det[\boldsymbol{C}(\tilde{\kappa}_1)]$ will have the same sign. However, if u_1 is included from the positive feedback loop, regardless of whether it is also part of the negative feedback loop, $\det[\boldsymbol{C}(\tilde{\kappa}_1)]$ will only represents negative feedback loops, and $\det[\boldsymbol{A}]$ and $\det[\boldsymbol{C}(\tilde{\kappa}_1)]$ will have opposite signs. Therefore, if u_1 is excluded from the positive feedback loop, it will increase upon inhibition its production, while if it is part of the positive feedback loop (whether or not it is also in the negative feedback loop) it will decrease if its production is inhibited. These constraints are summarized in Figure 4b.

4.2.3: Response of u_2

Conditions for the response of component u_2 to inhibition of component u_1 were defined in supplemental note 3, conditions 3.7 and 3.8. Writing these in terms of paths between u_1 and u_2 (see equation 3.9) the response of u_2 depends on the sign of

$$-\sum_{p_n \subseteq S_{p_n}} (-1)^n w(p_n) \det[\boldsymbol{C}(\tilde{\kappa}_n)] \sum_{j=1}^{N} \mathrm{C}[\boldsymbol{A}]_{j1} b_j, \quad (4.3)$$

where each summand contains a different path from u_1 to u_2. Written in this form, it is apparent that the response of u_2 to the inhibition of u_1 is again dependent on two topological features of the minimal system: the weight of the path from component u_1 to u_2 (given by the term $w(p_n)$) and whether the nodes excluded from this path support a positive feedback loop (given by $\det[\boldsymbol{C}(\tilde{\kappa}_n)]$).

If there only exists a single path from u_1 to u_2, there will only be a single non-zero term in Equation (4.3). As shown in the above analysis of the phase relationship (Section 4.1.2), the sign of the path $w(p_k)$ will be positive if u_1 and u_2 are in-phase and negative if out-of-phase. The only exception is when u_1 is excluded from the positive feedback loop but the path to u_2 passes into

or through the positive feedback loop, in which case the relationship between the nodes is reversed. As detailed in Equation (3.1), the relationship between the sign of det $[\boldsymbol{C}(\tilde{\kappa}_n)]$ and the feedback loops contained depends on the number of nodes in the system described by submatrix $\boldsymbol{C}(\tilde{\kappa}_n)$ (see Section 1). Again, considering all possible combinations of odd and even numbers of components in submatrices $\boldsymbol{C}(\tilde{\kappa}_n)$ and path $w(p_k)$, and given that $\sum_{j=1}^{N} \mathrm{C}[\boldsymbol{A}]_{j1} b_j$ has the same sign as det $[\boldsymbol{A}]$ (see Section 2), the term $-(\sum_{j=1}^{N} \mathrm{C}[\boldsymbol{A}]_{j1} b_j)(-1)^n \det[\boldsymbol{C}(\tilde{\kappa}_n)]$ will be positive if det $[\boldsymbol{C}(\tilde{\kappa}_n)]$ contains the destabilising positive feedback loop, and negative otherwise.

Therefore, considering all possible placements of u_1 and u_2 relative to the two loops of the minimal system it can be seen that if u_1 is in the positive feedback loop (and therefore the positive feedback loop is not found in submatrix $\boldsymbol{C}(\tilde{\kappa}_n)$), u_2 will decrease if it is in-phase with u_1, and increase if out-of-phase. However, if u_1 is excluded from the positive feedback loop, u_2 will increase if it is in-phase with u_1, and decrease if out-of-phase, as either the path to u_2 will pass from the negative feedback loop into the positive feedback loop, or this path will exclude components from the positive feedback loop. These constraints are summarized in Figure 4b.

It should be noted that in certain instances when u_1 and u_2 lie in both the positive and negative feedback loop, two paths can be traced from u_1 to u_2: one consisting of interactions only found in the positive feedback loop, and the other comprising ones only found in the negative feedback loop. There will therefore be two summands in Equation (4.3), one associated with each path, and they will be of opposing signs. Therefore, the response of u_2 to the inhibition of u_1 will depend on the relative weight of each path, and it can either increase or decrease.

It should be noted that while the response of u_2 to the inhibition of u_1 is not constrained by topology in these instances, it is coupled with the responses of other components in the system. Factoring out all coefficients shared between the two summands leaves

$$\left(-1\right)^{w-\nu(w^+)} w(p_{w^+}) \det[\boldsymbol{W}(\tilde{\kappa}_{w^+})] + \left(-1\right)^{w-\nu(w^-)} w(p_{w^-}) \det[\boldsymbol{W}(\tilde{\kappa}_{w^-})], \quad (4.4)$$

where matrix $\boldsymbol{W}$ is the submatrix $\boldsymbol{A}(\gamma_w)$ comprising the w components supporting the two paths defined by γ_w. The terms $w(p_{w^+})$ and $w(p_{w^-})$ give the weights of the paths through the positive and negative loops, respectively, $\nu(w^+)$ and $\nu(w^-)$ the numbers of components in the respective paths, and $\boldsymbol{W}(\tilde{\kappa}_{w^+})$ and $\boldsymbol{W}(\tilde{\kappa}_{w^+})$ the submatrices of $\boldsymbol{W}$ comprising the components excluded from the respective paths. This same sum is also left when considering the response

of u_1 to its own inhibition if it falls in both feedback loops, and shared terms are factored out of Equation (4.2). In both instances, if the weight through the positive feedback loop is greater than that through the negative feedback loop, that is

$$\left|(-1)^{w-\nu(w^+)}w(p_{w^+})\det[\boldsymbol{W}(\tilde{\kappa}_{w^+})]\right| > \left|(-1)^{w-\nu(w^-)}w(p_{w^-})\det[\boldsymbol{W}(\tilde{\kappa}_{w^-})]\right|,$$

then u_1 will decrease on its own inhibition, as will any in-phase components, with out-of-phase components increasing. However, when the inequality is reversed and u_1 increases on its own inhibition, the response of any component to which the two paths can be traced will be coupled, increasing if it is in-phase, and decreasing if out-of-phase.

4.3: Adding nodes to minimal topologies

In the above analysis of the criteria for a minimal topology (Section 4.1.1) we only considered strongly-connected networks, where the two feedback loops comprise all N components. For systems where the two loops only pass through a subset of components, if the remaining components respond passively (i.e. do not feed back into the system) each component will only add a single interaction. Like the strongly-connected networks these networks also have two loops and N+1 interactions.

These passive components can be wired back into the minimal RD 'core' by adding interactions from the passive components back to the core. If the weights of any additional interactions, or the weights of additional loops generated by them, are not excessively large, the criteria for DDI will still be met, and the phase relationship of the related not strongly-connected minimal topology will also be maintained. While the resulting topologies are not strictly minimal in terms of the number of loops or interactions, they comprise additional strongly-connected networks which satisfy the conditions for DDI. Moreover, as the removal of an interaction will either result in the system either no longer satisfying the criteria for DDI or no longer being strongly-connected, we will also consider such topologies as an additional form of minimal topology.

We will now consider the effect of inhibition on networks with additional components wired in outside of the RD 'core'. We first will consider the case where there is a single component u_1, external to the core, and the effect of inhibiting this component on its own levels, before

considering the effect of inhibiting u_1 on core components. We then consider the effect of external interactions on the core.

4.3.1: Effect on self

The addition of a single component external to the RD core will generally result in the addition of a single positive feedback loop to the system (we will discuss below the subset of cases where the addition of a single component results in the addition of two loops).

Inhibition of response

As for the minimal topologies (Section 4.2.1) when the response to u_1 is inhibited, the behaviour of u_1 depends on the sign of the sum in Equation (4.2). This sum will consist of a single term, and as before, the sign of this term depends in part on whether or not the submatrix $\boldsymbol{C}(\tilde{\kappa}_n)$ contains the destabilising core positive feedback loop, and also whether this loop supports positive or negative feedback. We will ask how the wiring of this loop relative to the core positive feedback loop, along with the weighting of the loop, determines the response to inhibition.

We will first consider when the feedback loop through u_1 includes components from the core positive feedback loop. In this case submatrix $\boldsymbol{C}(\tilde{\kappa}_n)$ contains only negative feedback loops and $(-1)^n \det[\boldsymbol{C}(\tilde{\kappa}_n)] / \det[\boldsymbol{A}]$ will be positive. If u_1 itself supports a positive feedback loop, condition (3.4) will be satisfied and u_1 will decrease on its own inhibition. Conversely, if u_1 supports a negative feedback loop, condition (3.3) will be satisfied and u_1 will increase on its own inhibition. These relationships are reversed if the loop through u_1 does not pass through any components in the core positive feedback loop. If this is the case, submatrix $\boldsymbol{C}(\tilde{\kappa}_n)$ will contain the core positive feedback loops and $(-1)^n \det[\boldsymbol{C}(\tilde{\kappa}_n)] / \det[\boldsymbol{A}]$ will be negative (otherwise conditions for DDI cannot be met — see Section 1). In this instance, if u_1 supports a positive feedback loop, condition (3.3) will now be satisfied and u_1 will increase on its own inhibition, while if u_1 supports a negative feedback loop, condition (3.4) will be satisfied and u_1 will decrease on its own inhibition.

Interestingly, the response of u_1 to its inhibition does not correlate directly with the feedback loop u_1 supports, but rather with the net feedback provided to the core positive feedback loop

(i.e. the weight the path from u_1 to a core positive feedback component multiplied by the weight of the return path). If u_1 supports a net positive feedback, it will decrease on its own inhibition, while if it provides a net negative feedback, it will increase on its own inhibition. These constraints are summarized in Figure 4d.

Inhibition of production

As demonstrated in Section 3, the response to the inhibition of production is dependent on the sign of det $[\boldsymbol{C}(\tilde{\kappa}_1)]$ relative to det $[\boldsymbol{A}]$ (condition (3.5) or (3.6)). As det$[\boldsymbol{A}]$ and det$[\boldsymbol{C}]$ only differ by the presence of the degradation coefficient c_1 in the first matrix term it follows that

$$1 = \frac{-(-1)^n w(\kappa_n)\,\det[\boldsymbol{C}(\tilde{\kappa}_n)] - c_1\,\det[\boldsymbol{C}(\tilde{\kappa}_1)]}{\det[\boldsymbol{A}]}.$$

In the above analysis of the inhibition of response, we demonstrated how network topology (i.e. the sign of the loop containing u_1, and how this feeds into the core RD network) determines the sign of $(-1)^n w(\kappa_n)\det[\boldsymbol{C}(\tilde{\kappa}_n)]/\det[\boldsymbol{A}]$. From these arguments, it follows that if u_1 supports a net positive feedback, $-c_1\,\det[\boldsymbol{C}(\tilde{\kappa}_1)]/\det[\boldsymbol{A}]$ must be negative. As $-c_1$ is negative, condition (3.6) will be satisfied and u_1 will decrease. However, if u_1 supports a net negative feedback, the sign of $-c_1\,\det[\boldsymbol{C}(\tilde{\kappa}_1)]/\det[\boldsymbol{A}]$ is not constrained and therefore both conditions (3.5) and (3.6) can be satisfied. Therefore, u_1 will decrease on the inhibition of its production if it provides a net positive feedback to the core positive feedback loop, but depending on the strength of the different feedback loops, u_1 will either increase or decrease when its production is inhibited if it provides a net positive feedback. These constraints are summarized in Figure 4d.

It should be noted that in some instances where u_1 feeds into and out of the core RD network at components which are found in both core positive and negative feedback loops, it is possible that a second loop supported by u_1, through components only found in the core negative feedback loop, will also exist. In this case the two terms describing alternate paths through the positive feedback loop and negative loop (see Section 4.4) will again remain after shared components are factored out. As discussed above, in the cases where the magnitude of the path through the negative feedback loop is greater than the path through the positive feedback loop, the relationships between the response of u_1 to its own inhibition and the feedbacks it supports described here will also be inverted.

4.3.2: Effect on core components

We will now consider the how inhibiting the external component u_1 affects a core component u_2. We will consider the effect of whether u_1 feeds directly into the positive or negative feedback loop of the core RD network, and on whether u_2 itself lies in the core positive or negative feedback loop. As for minimal systems (Section 4.2.2), u_2 will decrease on the inhibition of u_1 if the sign of the path from u_1 to u_2 is positive, unless the submatrix determinant $\det[\boldsymbol{C}(\tilde{\kappa}_n)]$ contains the positive feedback loop of the core RD network. Likewise, u_2 will increase if the path from u_1 to u_2 is negative, unless the path excludes the core RD network positive feedback loop.

If u_1 feeds into the core RD network through the positive feedback loop, $\det[\boldsymbol{C}(\tilde{\kappa}_n)]$ will not contain the core positive feedback loop. The response will therefore depend on the sign of $w(p_k)$, such that if u_1 itself supports a positive feedback loop, the weight of the path from u_1 to u_2 will be positive if u_1 and u_2 are in-phase, and negative if they are out-of-phase. Therefore, u_2 will decrease if it is in-phase with u_1 and increase if it is out of phase. The opposite will occur if u_1 is in a negative feedback loop, with the level of u_2 increasing if it is in-phase with u_1 and decreasing if it is out-of-phase.

We next consider the case when u_1 feeds into the core through the negative feedback loop. If u_2 is also found in this loop, and the path from u_1 does not pass through the core positive feedback, the sign of the path will be positive if the components are in-phase and negative if they are out-of-phase, provided u_1 supports a positive feedback loop (and therefore provides a net negative feedback to the core positive feedback loop). The reverse is true if u_1 supports a negative feedback loop (and thus a net positive feedback). As the core positive feedback components are found in $\det[\boldsymbol{C}(\tilde{\kappa}_n)]$, if u_2 is in-phase with u_1 it will decrease on inhibition if u_1 provides a net positive feedback, and out-of-phase components will increase, with the reverse true if u_1 provides a net negative feedback. The same is also true when u_1 feeds into the core negative feedback loop, but the path to u_2 passes into or through the core positive feedback loop. When the core positive feedback components are found no longer in submatrix $\boldsymbol{C}(\tilde{\kappa}_n)$ and therefore the sign of $\det[\boldsymbol{C}(\tilde{\kappa}_n)]$ is reversed, the relationship between the signs of the path from u_1 to u_2 and the phase relationship are now inverted by passing back into the core positive feedback loop, maintaining the above relationship.

Therefore, regardless of where the path from u_1 feeds into the core RD network, if u_1 provides a net negative feedback loop, u_2 will increase if it is in-phase with u_1, and decrease if it is out-of-phase. The opposite will be true if u_2 supports a net positive feedback. These constraints are summarized in Figure 4d. Again, there can be instances where two paths of opposing sign can be traced from u_1 to u_2 if u_1 feeds into a component found in both core loops and u_2 is also found in both loops. The response is again dependent on the sign of Equation (4.4), with the above responses inverted if the magnitude of the term relating to the path through the negative feedback loop is greater than those relating to the positive feedback loop, with all components receiving input from the two paths responding in a coupled manner.

4.3.3: Effect of adding external components to an RD system

Finally, we considered the effect adding external components to existing constraints on the system. We asked whether the addition of an external component could change the behaviours within the minimal RD core. As shown above, a major feature determining the response of a component in a minimal RD network either to its own inhibition, or the inhibition of another component, is whether or not various submatrices contain the destabilizing positive feedback loop of the core RD network. In some instances, the addition of loops can change the stability of these submatrices, either making stable submatrices unstable by adding a positive feedback loop, or making unstable submatrices stable by the addition of further negative feedback. However, it should be noted that as the various loops and paths that determine the behaviours within the core will still be present, only certain placements of feedback loops have such effects, and that they only affect certain components under particular parameterisations. There will still exists parameterisations where the responses described above (summarized in Figure 4b) are maintained.

The constraints applying to the addition of one external component will, therefore, apply to any number of external components, provided that the magnitudes of additional interactions are not sufficiently large to change the stability of any submatrices. This also opens up the possibility of considering potential interactions between external components u_1 and u_2 (for simplicity we will only consider the cases where the path between u_1 and u_2 passes through the core). The path will contain the path from u_1 to a core component, plus an additional interaction to u_2. Therefore, the response of u_2 to the inhibition of u_1 will be the same as that of the preceding core component in the path if the final interaction is positive, and the opposite if it is

negative. The same is true of the response of external u_2 to a core u_1. Consequently, if u_1 is involved in positive feedback (either as the core loop or as a source of additional positive feedback), then u_2 will decrease if it is in-phase with u_1, and increase if it is out-of-phase, while if u_1 provides negative feedback the reverse is true. As has been discussed above, when two paths can be traced from u_2 to u_1, if the path through the negative feedback loop has a greater weighting these relationships will be inverted coupled to other such components.

Taken together, the effects of inhibiting u_1 on itself, and on u_2 primarily depend on whether u_1 falls in the core positive feedback loop, or provides an additional net positive feedback, or whether it provides negative feedback. While for some parameterisations of some topologies, certain components will behave differently, these constraints on the behavior of minimal systems provide a framework to consider the behavior of RD networks in response to inhibition experiments.

References

Desoer, C. A. (1960). "The Optimum Formula for the Gain of a Flow Graph or a Simple Derivation of Coates' Formula." Proceedings of the IRE **48**(5): 883-889.

Marcon, L., X. Diego, J. Sharpe and P. Muller (2016). "High-throughput mathematical analysis identifies Turing networks for patterning with equally diffusing signals." Elife **5**.

Murray, J. D. (2003). Mathematical Biology, Berlin: Springer-Verlag.

White, K. A. J. and C. A. Gilligan (1998). "Spatial heterogeneity in three species, plant–parasite–hyperparasite, systems." Philosophical Transactions of the Royal Society of London. Series B: Biological Sciences **353**(1368): 543-557.